APPLIED SCIENCES AND ENGINEERING

Local soft niches in mechanically heterogeneous primary tumors promote brain metastasis via mechanotransduction-mediated HDAC3 activity

Kai Tang[1,2,3]†, Yufan Zheng[1,2,3]†, Guanshuo Hu[1,2,3], Ying Xin[1,2,3], Keming Li[1,2,3], Cunyu Zhang[1,2,3], Xi Chen[1,2,3], Bai Zhang[1,2,3], Xueyi Li[1,2,3], Bing Hu[1,2,3], Qiong Jia[4], Yong-ping Zheng[2,3], Mo Yang[3], Youhua Tan[1,2,3]*

Tumor cells with organ-specific metastasis traits arise in primary lesions with substantial variations of local niche mechanics owing to intratumoral heterogeneity. However, the roles of mechanically heterogeneous primary tumor microenvironment in metastatic organotropism remain an enigma. This study reports that persistent priming in soft but not stiff niches that mimic primary tumor mechanical heterogeneity induces transcriptional reprogramming reminiscent of neuron and promotes the acquisition of brain metastatic potential. Soft-primed cells generate brain metastases in vivo through enhanced transendothelial migration across blood-brain barrier and brain colonization, which is further supported by the findings that tumor cells residing in local soft niches of primary xenografts exhibit brain metastatic tropism. Mechanistically, soft niches suppress cytoskeleton-nucleus–mediated mechanotransduction, which promotes histone deacetylase 3 activity. Inhibiting histone deacetylase 3 abolishes niche softness-induced brain metastatic ability. Collectively, this study uncovers a previously unappreciated role of local niche softness within primary tumors in brain metastasis, highlighting the significance of primary tumor mechanical heterogeneity in metastatic organotropism.

INTRODUCTION

Tumor metastasis is not random but exhibits organ preference or organotropism (*1*), including the brain, bone, lung, and liver. Multiple types of cancer—such as breast, lung, colorectal, skin, and renal cell cancer—choose brain as their common metastatic site (*2*). Brain metastasis arises in ~20% of all patients with cancer and usually leads to neurological dysfunctions and devastating prognosis without effective therapeutic options (*3*, *4*). In particular, brain metastases occur in 10 to 30% of patients with metastatic breast cancer, with a median overall survival of 8.7 months (*4*, *5*). Further, primary and the matched metastatic tumors share most of the somatic mutations and gene expression profiles (*6*). The gene expression patterns of primary lesions can predict the metastatic risk in specific organs (*7*). Transforming growth factor–β (TGF-β) in primary tumors facilitates breast cancer lung metastasis via Smad-ANGPTL4 signaling pathway (*8*). The presence of CXCL12 and insulin-like growth factor 1 (IGF1) in the primary breast tumor promotes Src-dependent bone metastasis (*9*). These findings suggest that tumor cells with the ability to colonize specific organs may already exist in the primary site before dissemination (*1*). Therefore, unveiling the molecular mechanisms within primary tumor microenvironment is essential for the prediction of metastatic pattern and development of therapeutic strategies against brain metastases.

Despite the critical roles of biochemical mechanisms in organotropism [e.g., TGF-β (*8*), Src signaling (*9*), exosome (*10*), and cytokines (*11*)], cells can perceive mechanical cues from their microenvironment via integrin-mediated mechanotransduction, and the significance of primary tumor mechanics in metastasis has been increasingly appreciated (*12*): Excessive extracellular matrix (ECM) deposition and crosslinking increase breast tumor rigidity that promotes invasion through integrin-mediated focal adhesion (*13*); stiff tumors facilitate nuclear translocation of Twist1 and epithelial-mesenchymal transition (EMT) to promote metastasis (*14*); breast tumor stiffness regulates the expression and splicing of Mammalian Enabled (MENA) and enhances cancer cell contractility and intravasation (*15*); tumor mechanics activate cellular communication network factor 1 (CCN1)/β-catenin/N-cadherin signaling in endothelial cells, which facilitate their interactions with tumor cells and promote metastasis (*16*). Most of these studies have ignored the substantial variations of local niche stiffness within primary tumors, which could be induced by considerable intratumoral heterogeneity, a hallmark of cancer (*17*). Yet, the influence of primary tumor mechanical heterogeneity on metastasis remains less investigated: Soft regions in primary tumors facilitate breast cancer cell proliferation, while stiff regions promote angiogenesis and migration (*18*); stiff niches in hepatocellular carcinoma enhance tumor stemness and drug resistance, and soft niches promote cell proliferation (*19*); the spatial transcriptomics analysis shows the correlation between local niche stiffness and EMT markers in primary breast tumors (*20*). Furthermore, little attention has been paid to the effects of the mechanical microenvironment on organotropism and brain metastasis: The proliferation and migration of breast cancer cells with different organotropism correlate with the stiffness of the metastasized organs (*21*); the organotropism of breast and ovarian cancer cells is maximized on differential matrix rigidity, which depends on actomyosin tension (*22*); substrate rigidity affects the cluster size-dependent proliferation of breast cancer brain metastatic cells (*23*); stiff substrates induce the transition of tumor cells to an osteoclastic phenotype and promote osteolytic bone metastasis (*24*, *25*); stiff and soft matrices facilitate the

[1]The Hong Kong Polytechnic University Shenzhen Research Institute, Shenzhen 518057, China. [2]Research Institute of Smart Ageing, The Hong Kong Polytechnic University, Kowloon, Hong Kong, China. [3]Department of Biomedical Engineering, The Hong Kong Polytechnic University, Kowloon, Hong Kong, China. [4]Department of Oncology, Nanjing First Hospital, Nanjing Medical University, Nanjing, China, 210006.
*Corresponding author. Email: youhua.tan@polyu.edu.hk
†These authors contributed equally to this work.

migration and proliferation of bone and lymphatic metastatic cells in prostate cancer (*26*). Nevertheless, how mechanically heterogenous primary tumors influence brain metastasis remains poorly understood.

To address this question, we characterized the stiffness distribution in primary breast tumors and explored the influence of local soft and stiff niches on breast cancer brain metastasis. The mechanistic study unveiled the roles of mechanotransduction-mediated histone deacetylase 3 (HDAC3) activity in niche softness-induced brain metastasis. Our findings discovered the pivotal impact of local niche softness within primary tumors on brain metastasis and elucidated the underlying molecular mechanisms, highlighting the significance of mechanically heterogenous primary lesions in metastatic organotropism.

RESULTS

Soft niches induce transcriptomic reprogramming reminiscent of neuron and promote brain metastatic potential

Primary breast tumors are typically fibrotic with abundant collagen and thus have been assumed to become stiffened as a whole in most previous studies (*27*, *28*). However, as a hallmark of cancer, intratumoral heterogeneity could lead to substantial variations of local niche mechanics within primary tumors, varying from around 0.2 to 45 kPa as we measured using ultrasound shear-wave elastography (Fig. 1A), which recapitulated the stiffness variation within human breast cancer biopsies (from ~0.1 to 20 kPa) (*29*). To determine the influence of primary tumor mechanical heterogeneity on organotropism, human breast cancer cells were continuously primed on 0.6 and 35 kPa of polyacrylamide (PA) hydrogels coated with collagen I that mimicked local soft and stiff niches within the primary lesion (fig. S1A). Most of brain metastasis-related genes were not significantly altered within the first two passages, irrespective of niche stiffness, and notably up-regulated from passage 5 to 10 (i.e., 30 days) in soft but not stiff niches, which resembled the organotropic gene signature of MDA-MB-231 derivatives with brain metastatic tropism (MDA231-BrM2-831 or 231-BrM) (Fig. 1, B and C). The levels of these genes were not further enhanced after additional priming in soft niches (fig. S1B). We thus defined breast cancer cells after mechanical priming on 0.6 and 35 kPa of gels for 10 passages as soft- and stiff-primed cells. Bone metastasis–related genes were down-regulated in soft-primed cells compared to parental, bone metastatic (MDA-BoM-1833 or 231-BoM), and stiff-primed cells (fig. S1C).

Further RNA sequencing (RNA-seq) analysis identified abundant differentially expressed genes (DEGs) and considerable alterations in transcriptional signature of soft-/stiff-primed breast cancer cells (fig. S1, D and E), including the up-regulation and down-regulation of brain and bone metastasis genes in soft-primed cells (Fig. 1D and fig. S1, F to H). Bioinformatic analyses of soft-primed cells revealed the enrichment of the pathways related to neuron and central nervous system (Fig. 1, E and F, and fig. S2, A and B), brain cell–specific signature (fig. S2, C and D), and brain metastases (Fig. 1G and fig. S2E). Similar transcriptomic reprogramming was also observed in another breast cancer cells SUM159 after priming in soft and stiff niches (fig. S2, F to I) (*25*). In addition, mechanical priming up-regulated brain metastasis genes in another breast cancer cells 4T1 and tumor cells on fibronectin-coated soft gels (fig. S2, J and K). This effect was not ascribed to random genetic drift after extended priming in different mechanical microenvironments because similar treatment on tissue culture plastic (TCP) did not have notable influence on brain metastasis genes (fig. S2L). These results implicate that soft niches induce transcriptomic reprogramming of tumor cells reminiscent of neuron and this neuronal mimicry may potentiate the brain metastatic ability (*30*, *31*), which may not rely on specific ligands and cell lines.

We next asked whether soft-primed tumor cells acquired brain metastatic ability. To establish overt brain metastases, disseminated tumor cells must navigate through multiple metastatic steps, including survival in circulation, extravasation through blood-brain barrier (BBB), and outgrowth in the brain microenvironment (*2*). Upon intravasation, circulating tumor cells are required to survive blood shear stress. To mimic this milieu, mechanically primed tumor cells were circulated in a microfluidic system that could generate pulsatile shear stress (*32*). Soft-primed cells survived better than stiff-primed and parental cells under both shear stress and suspension (fig. S3, A and B). After survival in circulation, tumor cells need to re-adhere to brain microvascular endothelium before extravasation. Soft-primed cells adhered better to brain endothelium but not human umbilical vein endothelial cell monolayer (Fig. 1, H and I, and fig. S3C), which might be elicited by the up-regulation of cell adhesion molecules on soft-primed cells that can physically interact with brain endothelium (fig. S3, D and E). Extravasation across BBB limits the success rate of brain metastasis (*33*). To investigate this ability, we developed an in vitro BBB model with brain microvascular endothelial cells and astrocytes on the top and bottom of a Transwell membrane (fig. S3F) (*33*). Soft-primed cells and 231-BrM exhibited enhanced BBB transmigration ability compared to parental and stiff-primed cells (Fig. 1, J and K), which was also observed in soft-primed 4T1 cells (fig. S3G). Cyclooxygenase 2 (COX2) and its end-product prostaglandin E2 (PGE2) critically affect BBB transmigration (*33*, *34*). Soft priming up-regulated COX2 and the secretion of PGE2 (fig. S3, H and I). Pharmacologic inhibition of COX2 abrogated BBB transmigration of soft-primed tumor cells (fig. S3J). Note that tumor cells can generate contractile force to interact with brain endothelium (*35*, *36*), which may mechanically alter the endothelial gap by changing endothelial mechanics to promote extravasation (*37*). However, the potential mechanisms underlying the mechanical cross-talk between soft-primed tumor cells and brain endothelium remain unclear. Upon the arrival at brain site, disseminated tumor cells must adapt to the brain microenvironment to generate macroscopic metastases (*38*). We examined the mechano-adaptation ability of tumor cells on soft matrices that recapitulated the softness of brain tissue, in which soft-primed tumor cells exhibited enhanced adhesion, elongated cell shape, and increased spreading area and proliferation (fig. S4, A to E). Further, soft-primed cells had enhanced/reduced migration and invasion ability in soft/stiff microenvironments (fig. S4, F to H). No significant difference was observed in the survival of these cells on soft matrices (fig. S4I). Further, three-dimemsional (3D) hyaluronic acid (HA) hydrogels with the stiffness of 1 kPa were used to mimic the brain microenvironment (fig. S4J). Soft-primed cells exhibited enhanced survival and proliferation ability (Fig. 1, L and M, and fig. S4K). Furthermore, multiple cytokines linked to brain colonization, including Serpins, were up-regulated in soft-primed cells (fig. S4, L and M) (*39*). Serpins are known to promote tumor cell survival in the brain (*40*). Soft-primed tumor cells had elevated levels of Serpins (fig. S4, L and M) and secreted more Serpin B2 (fig. S4N), which might further support their remarkable brain colonization ability after plating in mouse brain slices (Fig. 1, N and O). All these results demonstrate that soft priming enhances the

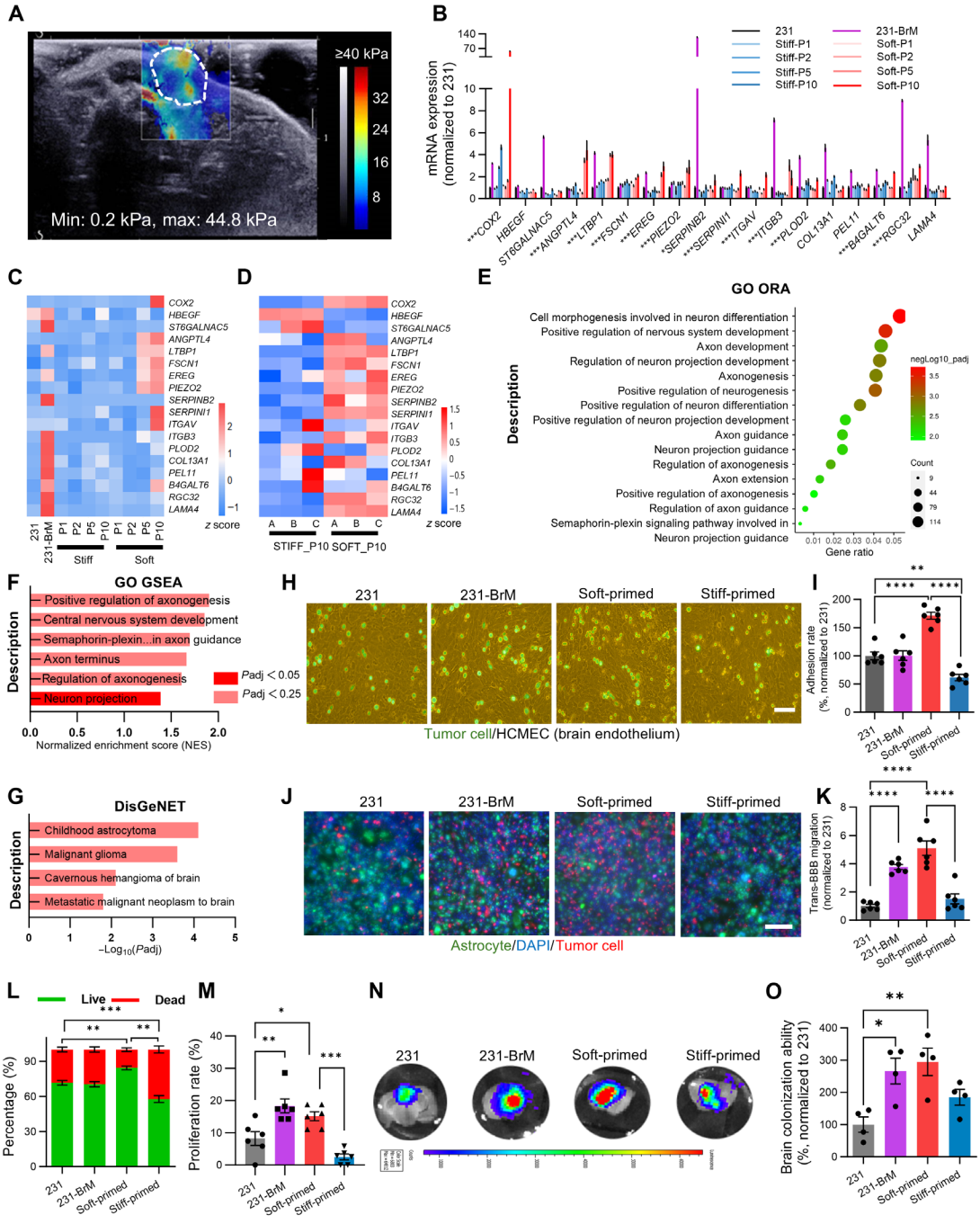

Fig. 1. Soft niches induce transcriptomic reprogramming reminiscent of neuron and promote brain metastatic potential. (**A**) Representative image of ultrasound elastography measurement. White dashed line indicated tumor boundary. (**B**) Reverse transcription quantitative polymerase chain reaction (RT-qPCR) analysis of brain metastasis–related genes in 231 cells after priming in soft/stiff niches for 1, 2, 5, and 10 passages, respectively. $n = 3$. The symbol (star) represented the statistical significance between Soft-P10 and 231. (**C**) Heatmap of the expressions of brain metastasis-related genes in (B). Colors represented the scaled expression levels after *z*-score normalization. (**D**) Heatmap of the expressions of brain metastasis–related genes in RNA-seq datasets. (**E**) Gene Ontology (GO) over-representation analysis (ORA) of up-regulated DEGs and (**F**) gene set enrichment analysis (GSEA) result in soft-primed cells compared with stiff-primed cells. Significantly enriched neuron-associated pathways were shown. (**G**) DisGeNET enrichment analysis of up-regulated genes in soft-primed cells compared with stiff-primed cells. Brain tumor–associated terms were significantly enriched. (**H**) Representative images of tumor cells adhering to the brain endothelial layer. Scale bar, 100 μm. (**I**) Adhesion rate of tumor cells on the brain endothelial layer. $n = 6$. (**J**) Representative images of BBB transmigration assay in 231, 231-BrM, soft-primed cells, and stiff-primed cells. Scale bar, 200 μm. (**K**) Quantification of transmigrated cells in (J). $n = 6$. (**L**) Percentages of live/dead cells and (**M**) proliferation rate of 231, 231-BrM, soft-primed cells, and stiff-primed cells after seeding into 3D soft HA gels for 24 hours. $n = 8$ (L) and 6 (M). (**N**) Bioluminescence imaging and (**O**) quantification of 231, 231-BrM, soft-primed cells, and stiff-primed cells cultured on brain slices for 48 hours. $n = 4$. One-way analysis of variance (ANOVA) with Dunnett test in (B) and Tukey test in [(I), (K) to (M), and (O)]. $^*P < 0.05$, $^{**}P < 0.01$, $^{***}P < 0.001$, and $^{****}P < 0.0001$. Data presented as the means ± SEM. DAPI, 4′,6-diamidino-2-phenylindol.

mechano-adaptation of tumor cells to brain-mimicking microenvironments. In summary, all these findings conclude that soft niches induce transcriptomic reprogramming reminiscent of neuron and promote brain metastatic potential in vitro.

Soft priming potentiates brain metastatic tropism through enhanced BBB transmigration and brain colonization in vivo

We next tested the brain metastatic potential of soft-primed breast cancer cells in vivo. After intracardiac inoculation, soft-primed tumor cells developed brain metastasis in 75% of mice, which was reduced to 40 and 20% for stiff-primed and parental cells (Fig. 2A), respectively. As a positive control (*33*), 231-BrM cells had the ability to initiate brain metastasis. Soft-primed tumor cells not only induced high incidence of brain metastasis but also generated larger secondary tumors in the brain (Fig. 2, B and C). Furthermore, the analysis of brain metastasis-free survival curve indicated the robust brain metastatic potential of tumor cells in vivo after soft priming (Fig. 2D). Ex vivo imaging further confirmed that soft priming promoted the growth of brain metastases and the number of metastatic foci in the brain (Fig. 2, E and F, and fig. S5A). These results demonstrate that mechanical priming in soft niches alters organotropic preference and promotes breast cancer brain metastasis in vivo.

After intracardiac inoculation, tumor cells can metastasize to the brain by disseminating into brain vasculature, transmigrating across BBB, and generating brain colonization, the efficiencies of which limit the incidence of brain metastasis. Previous studies report that the majority of circulating tumor cells entrapped in the brain capillary beds escape the arrest within the first 3 days (*41*). There was no significant difference in initial arrest at the brain site among soft-/stiff-primed cells and parental cells within the first 3 days after intracardiac inoculation (Fig. 2, G and H), which was further confirmed by ex vivo bioluminescence signal from mice brain extracted at day 3 (fig. S5B). These results suggest that soft priming facilitates brain metastasis probably not through preferential arrest of specific tumor cells in brain microcapillary beds. We then explored the ability of these cells to extravasate across the BBB. Mouse brain tissues were fixed and sectioned to count the number of tumor cells that were arrested within brain capillaries and underwent or completed the extravasation at day 3 after intracardiac inoculation (Fig. 2, I and J). More parental and stiff-primed cells were entrapped in brain microvessels (Fig. 2K), while larger portions of soft-primed cells and 231-BrM were extravasating across the BBB and had completed this process and infiltrated into the brain parenchyma (Fig. 2, L and M). Last, we investigated brain colonization ability of these mechanically primed tumor cells. After intracranial implantation (fig. S5C), soft-primed cells and 231-BrM exhibited much higher brain colonization ability (Fig. 2N) and generated larger brain metastases than stiff-primed and parental cells (Fig. 2O). Notably, the brain metastases generated by 231-BrM and soft-primed cells were visibly vascularized (Fig. 2P), indicating increased angiogenesis. These generated brain metastases showed much larger colonization areas and increased proliferation (Ki-67 positive) (Fig. 2, Q to S). All these findings indicate that soft priming promotes breast cancer brain metastasis through enhanced BBB extravasation and brain colonization in vivo.

Soft priming alters mechanical phenotypes and instills mechanical memory

Cell mechanical phenotype is considerably altered during metastasis and associated with malignancy (*42*). Our latest studies have further demonstrated that the reduction of cell mechanics during progression drives tumor growth, migration, and invasion (*43*, *44*). We thus characterized the mechanical phenotypes of these soft-/stiff-primed tumor cells. Soft-primed cells showed significantly higher stiffness in soft niches compared to other cells (fig. S5D), which was supported by the enhanced level of F-actin (fig. S5, E and F). These cells exhibited reduced F-actin on TCP (fig. S5F). Unlike the parental group, soft-primed cells had reduced cortical actin filaments in soft but not stiff niches (fig. S5G). Compared to parental cells, soft-primed cells exhibited higher phosphorylation of myosin light chain in soft niches but lower level on TCP (fig. S5, H and I). Consistently, these cells also generated enhanced contractile forces than stiff-primed and parental cells on soft substrates (fig. S5, J and K). Collectively, these findings suggest that soft-primed cancer cells exhibit elevated F-actin and myosin activation and thus cellular biomechanics in soft niches.

We next investigated the mechanical plasticity of soft-primed cells when being plated on TCP. Starting from day 3, these cells altered from less spreading and round shape to elongated and spreading morphology that resembled that of 231-BrM (fig. S6, A to D). Further, the stiffness of soft-primed cells was lower than that of 231 cells on TCP at day 14 (fig. S6E). We further examined the plasticity of brain metastatic potential when the mechanical microenvironment was altered. The levels of brain metastasis-related genes in soft-primed cells decreased gradually but were still higher than that in parental cells after 14 days on TCP (fig. S6F), indicating that soft priming might instill mechanical memory. Notably, soft-primed breast cancer cells after culture on TCP for 30 days rapidly up-regulated the brain metastasis gene signature within only two passages in soft niches (fig. S6G), much faster than the acquisition of this gene pattern in parental cells. These cells exhibited advantages in the proliferation on soft matrices and propensity to colonize the brain (fig. S6, H and I) despite no difference in BBB transmigration (fig. S6J). In summary, these findings suggest that soft niches prime mechanical phenotypes of breast cancer cells and instill mechanical memory, which may enable tumor cells to retain brain metastatic characteristics even after experiencing diverse mechanical microenvironments during the metastatic process.

In vitro soft priming confers brain metastatic ability through phenotypic reprogramming

The acquisition of brain metastatic ability after mechanical priming in soft niches could be likely explained by two possible mechanisms: clonal selection of a pre-existing subpopulation of tumor cells with brain metastatic ability and/or reprogramming of tumor cells without this ability into brain metastatic cells. To test these possibilities, we used single-cell cloning technique to generate genetically homogeneous progenies with low and high levels of brain metastasis gene signature [single cell population (SCP)-Low and SCP-High] (fig. S7, A and D). Soft priming significantly up-regulated brain metastasis genes in SCP-Low subclones (fig. S7B) and facilitated the transmigration across BBB, brain colonization, and proliferation on soft matrices (fig. S7C, E and F). These results indicate that mechanical priming in soft niches reprograms a subpopulation of tumor cells into brain metastatic phenotype. As expected, SCP-High cells exhibited enhanced ability to transmigrate BBB, colonize brain tissue, and proliferate on soft substrates but not TCP compared to SCP-Low cells (fig. S7, E and G to I). To consider the reciprocal effects on clonal competition, we labeled SCP-High and SCP-Low cells with green and red dye, respectively, and cocultured them on soft matrices and TCP. Consistently, SCP-High cells proliferated significantly

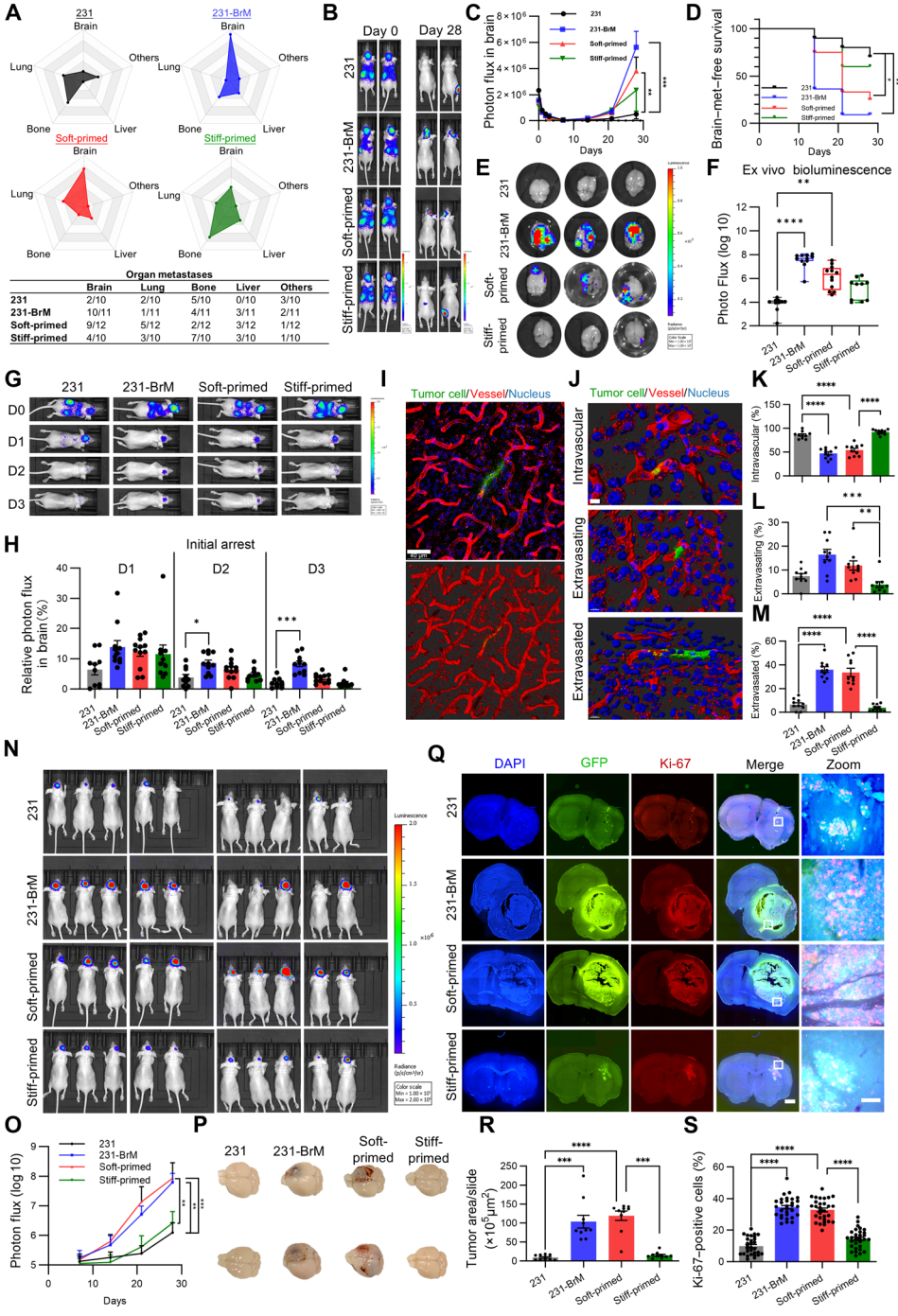

Fig. 2. Soft priming potentiates brain metastatic tropism through enhanced BBB transmigration and brain colonization in vivo. (**A**) Radar charts and the table showing the incidence of metastasis in different organs at day 28 after intracardiac injection of 231, 231-BrM, soft-primed cells, and stiff-primed cells. $n = 10$ (231, stiff-primed cells), 11 (231-BrM), and 12 (soft-primed cells). (**B**) Representative bioluminescence imaging of tumor metastasis at days 0 and 28 after intracardiac injection. (**C**) Quantification of photon flux in brain tissue in (B). (**D**) Kaplan-Meier analysis of brain metastasis-free survival in (B). (**E**) Representative bioluminescence imaging of brain metastatic lesions ex vivo in (B). (**F**) Quantification of photon flux in (E). $n = 10$. (**G**) Representative bioluminescence imaging at days 0, 1, 2, and 3. (**H**) Quantification of photon flux in the brain area in (G). (**I**) Representative confocal imaging (top) and 3D reconstruction (bottom) showing tumor cells trapped in the brain capillaries at day 3 post-intracardiac injection. Scale bar, 40 μm. (**J**) Representative 3D reconstruction showing intravascular, extravasating, and extravasated tumor cells at day 3. Scale bar, 100 μm. Quantification of intravascular (**K**), extravasating (**L**), and extravasated (**M**) tumor cells in (J). $n = 10$. (**N**) Bioluminescence imaging at day 28 after intracranial injection. (**O**) Quantification of photon flux in the brain area in (N). $n = 10$. (**P**) Representative images of brain lesions and (**Q**) immunofluorescence images of Ki-67 staining of coronal brain sections at day 28 after intracranial injection. Scale bars, 1 mm and 100 μm (zoom). (**R**) Quantification of brain metastatic lesion size in (Q). $n = 10$. (**S**) Quantitation of Ki-67–positive tumor cells in (Q). $n = 30$. Kruskal-Wallis test in [(C), (F), (H), (O), and (R)]. Log-rank test in (D). One-way ANOVA with Tukey's test in [(K) to (M)] and (S). $^*P < 0.05$, $^{**}P < 0.01$, $^{***}P < 0.001$, and $^{****}P < 0.0001$. Data presented as the means ± SEM.

faster than SCP-Low cells on soft matrices but not TCP (fig. S7, J and K), suggesting the possibility of clonal selection of a subpopulation with brain metastatic potential and proliferative advantage in local soft niches, which warrants further investigation using the barcode lineage-tracking system (*45*). Collectively, these findings suggest that soft niches promote brain metastatic ability in vitro through phenotypic reprogramming.

HDAC3 is required for niche softness-induced brain metastasis and brain colonization of soft-primed tumor cells

The mechanical milieu can influence gene expression and cellular function through epigenetic modifications (*46*, *47*). The RNA-seq analysis revealed the enrichment of chromatin and histone modification in soft-primed tumor cells, particularly histone deacetylation and HDACs (Fig. 3, A and B, and fig. S8, A and B). Further bioinformatic analysis implicated the involvement of class I HDACs (HDAC1, 2, 3, and 8) in the regulatory networks (fig. S8, C and D), which are known to catalyze histone deacetylation, leading to chromatin condensation (*48*). This can be characterized by the chromatin condensation parameter (CCP) within the nuclei (*49*). Soft-primed cells exhibited increased heterochromatin and CCP values compared to parental and stiff-primed cells (fig. S8, E and F), which might be mediated by higher HDAC activity (Fig. 3C). We further investigated the roles of HDAC activity in brain metastasis. Pharmacologic inhibition of HDACs with vorinostat (SAHA) or trichostatin A (TSA) in soft-primed cells reduced chromatin condensation (fig. S9, A and B) and significantly down-regulated brain metastasis genes, BBB transmigration ability, brain colonization, and proliferation on soft matrices (fig. S9, C to H). Similar findings were also observed in soft-primed 4T1 cells and 231-BrM cells (fig. S9, I to K, and fig. S12, C and D). On the other hand, the inhibition of histone acetylases in parental cells enhanced chromatin condensation and BBB transmigration but had no promotive effects on the brain metastasis gene signature, brain colonization, or cell proliferation on soft matrices (fig. S10, A to E). These results suggest that histone deacetylation may be required but not sufficient in driving brain metastasis.

To explore the roles of HDAC activity in niche softness-induced brain metastasis, parental tumor cells were primed in soft niches with TSA. The pharmacologic inhibition of HDACs diminished the brain metastatic gene signature, BBB transmigration, brain colonization, and proliferation on soft matrices (Fig. 3, D to F, and fig. S11A), suggesting that HDAC activity is necessary for the acquisition of brain metastatic ability in soft niches. We then attempted to identify the specific HDAC functioning in soft priming. Knockdown of individual class I HDAC in soft-primed cells showed that only silencing HDAC3 significantly abolished brain metastatic functions (fig. S11, B to F), suggesting the potential roles of HDAC3. Moreover, clinical data showed that the mRNA level of HDAC3 in primary tumors of breast cancer patients with brain metastasis was higher than that in primary tumors of patients without brain metastasis (Fig. 3G). In breast cancer patients, the mRNA level of HDAC3 in brain metastases was higher than that in bone metastases (Fig. 3H). To test whether HDAC3 was required for the niche softness-induced acquisition of brain metastatic capability, a selective HDAC3 inhibitor, RGFP966, was used to treat parental cells during persistent priming in soft niches. Notably, soft priming enhanced HDAC3 protein expression, HDAC3 phosphorylation, and activity (Fig. 3, I and J). These findings are consistent with several recent reports showing the up-regulation of HDAC3 on soft matrices (*50*, *51*). The inhibition of HDAC3 abolished the emergence of niche softness-induced brain metastatic phenotype, represented by the reduced BBB transmigration, brain colonization, and proliferation on soft matrices (fig. S11, G to J). To exclude the potential off-target effect of pharmacologic inhibition, an enzymatic inactive mutant of HDAC3 (S424A) was constructed. This mutant was validated (fig. S11K) and used to transfect breast cancer cells, which were further primed in soft niches. Inactivation of HDAC3 enzymatic activity abolished the acquisition of brain metastatic potential in soft niches (Fig. 3, K and L), which was similar to the findings of pharmacologic inhibition.

The expression and phosphorylation level of HDAC3 were increased in 231-BrM cells (fig. S12, A and B). HDAC3 inhibition also disrupted the BBB transmigration and brain colonization of 231-BrM cells (fig. S12, C and D). However, the overexpression of HDAC3 alone did not consistently promote the brain metastatic phenotype (fig. S12, E to K). Together, these findings suggest that HDAC3 activity is required for niche softness-induced brain metastasis.

Previous studies have shown that when patients are diagnosed with cancer for the first time, there are varying levels of incidence rate of metastasis in different types of cancer (*52*), suggesting that it is likely that tumor cells with organotropic potential may already leave the primary lesion and disseminate to secondary sites at the time of first diagnosis. We next assessed the therapeutic potential of HDAC3 in preventing the formation of macroscopic brain metastases. In line with the results of HDAC inhibition (fig. S9, C to J), the pretreatment of soft-primed breast cancer cells with RGFP966 compromised BBB transmigration and reduced brain colonization in vitro and proliferation on soft substrates (fig. S13, A to C). Because RGFP966 has the ability to penetrate BBB (*53*), we further investigated whether it could effectively reduce the incidence of brain metastasis and inhibit brain colonization in vivo. Toward this goal, soft-primed breast cancer cells were inoculated into the left ventricles of nude mice, which were administrated with RGFP966 (Fig. 4A). We found that RGFP966 treatment significantly increased the brain metastasis-free survival in a dose-dependent manner (Fig. 4, B and C). High-dose treatment effectively suppressed the outgrowth of brain metastases (Fig. 4, D and E). Notably, this treatment reduced metastases not only in the brain but also in the whole body (Fig. 4E), suggesting a broad inhibitory effect of HDAC3 inhibition on metastasis. The suppressive effect was further supported by the significant reduction in the proliferation of brain metastatic cells, brain tumor burden, and the number of macroscopic lesions (Fig. 4, F to H). Together, these results conclude that targeting HDAC3 has potential therapeutic effects on preventing the generation of macroscopic brain metastases.

The repressed mechanotransduction in soft niches promotes HDAC3-mediated brain metastasis

Cells can perceive mechanical milieu through integrin-mediated mechanotransduction (*12*, *13*), which may further regulate HDAC3 activity and cellular functions. We thus explored the roles of cytoskeleton-mediated cellular mechanosensing in niche softness-induced brain metastasis. To intervene in the mechanotransduction process, parental breast cancer cells were continuously primed in soft niches, while actin cytoskeleton and Rho activity were activated by jasplakinolide (Jas) and narciclasine (Narci) (Fig. 5A), respectively. Jas notably antagonized HDAC3 activity, partially rescued the brain metastatic gene signature, and significantly impaired BBB transmigration, colonization in brain slices, and proliferation on

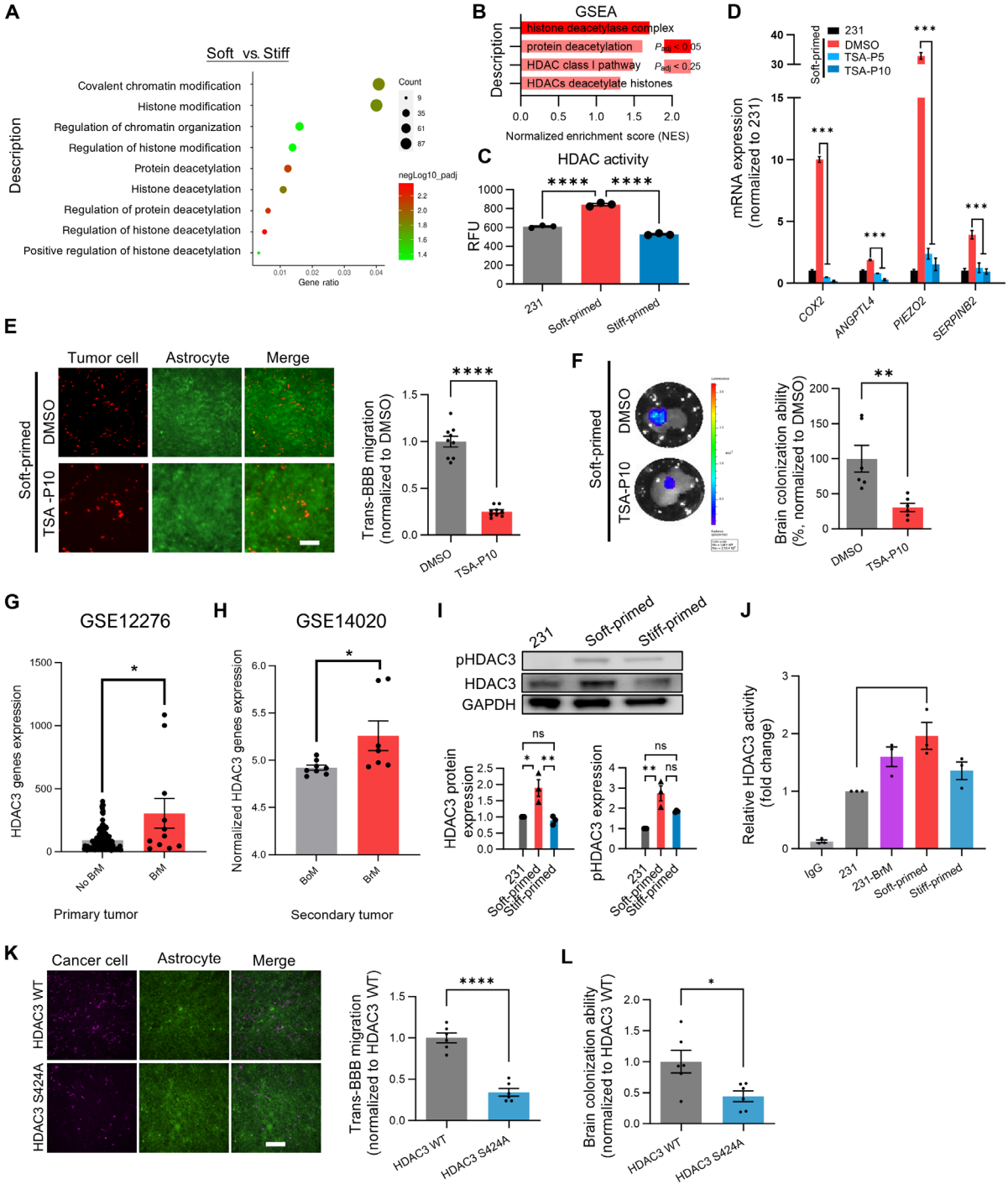

Fig. 3. HDAC3 is required for niche softness-induced brain metastasis and brain colonization of soft-primed tumor cells. (**A**) GO ORA of up-regulated DEGs in soft-primed cells compared with stiff-primed cells. The Cleveland plot shows the enrichment of chromatin remodeling–associated pathways. (**B**) GSEA of deacetylation-associated gene sets enriched in soft-primed cells compared with stiff-primed cells. RFU, relative fluorescence units. (**C**) HDAC activity measurement. $n = 3$. (**D**) Expressions of brain metastasis–related genes in tumor cells on soft gels in the presence and absence of TSA for 5 and 10 passages. $n = 3$. (**E**) BBB transmigration of tumor cells with or without TSA during soft priming. Scale bar, 200 μm. $n = 9$. (**F**) Bioluminescence imaging and quantification of the colonization of tumor cells with or without TSA during soft priming on brain slices. $n = 6$. (**G**) Expression of HDAC3 in primary breast tumors in patients with or without brain metastasis. $n = 143$ (No BrM) and 11 (BrM). (**H**) Expression of HDAC3 in brain/bone metastases of patients with breast cancer. $n = 7$ (BrM) and 8 (BoM). (**I**) Western blotting and quantification of HDAC3 expression and phosphorylation in 231, soft-primed, and stiff-primed cells. One-way ANOVA with Dunnett test, $n = 3$. (**J**) HDAC3 activity in 231, 231-BrM, soft-primed cells, and stiff-primed cells. $n = 3$. (**K**) BBB transmigration and (**L**) brain colonization of tumor cells with HDAC wild type (WT) or HDAC3 S424A after soft priming. $n = 6$. One-way ANOVA with Tukey's test in (C) and Dunnett test in [(D), (I), and (J)]. Two-tailed unpaired *t* test in [(E), (K), and (L)]. Mann-Whitney test in [(F), (G), and (H)]. $^*P < 0.05$, $^{**}P < 0.01$, $^{***}P < 0.001$, and $^{****}P < 0.0001$. Data presented as the means ± SEM.

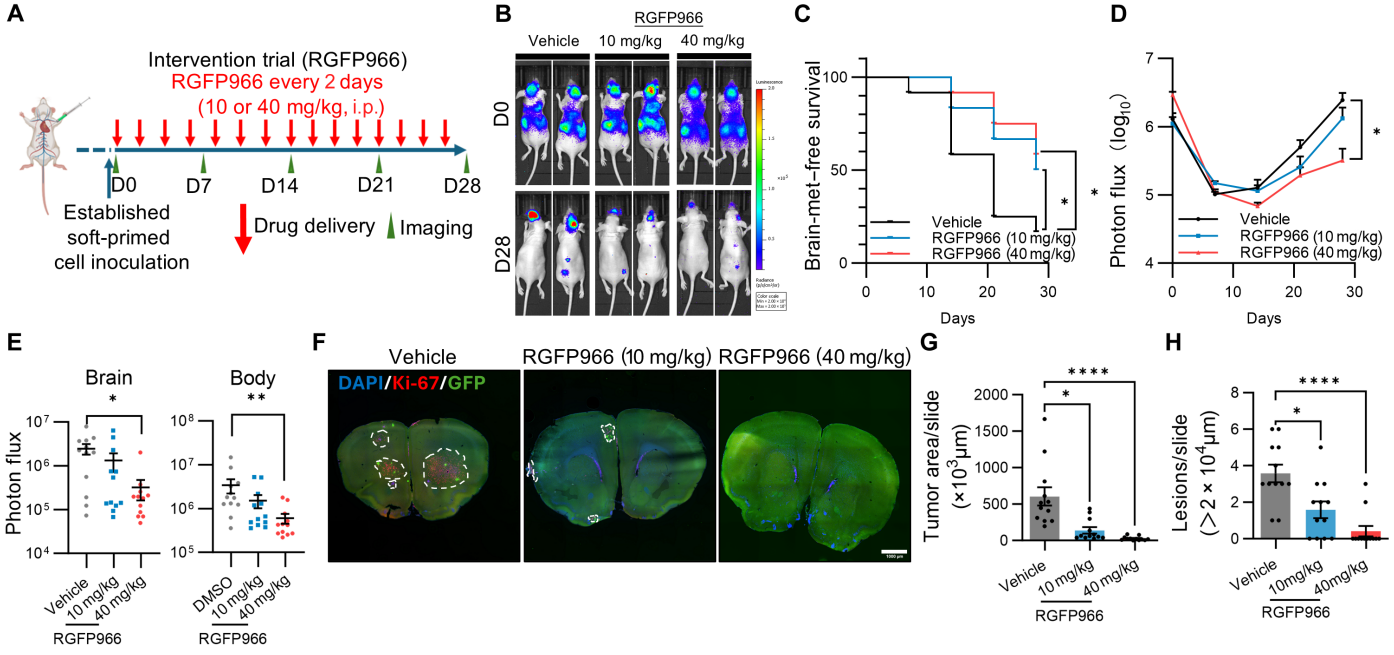

Fig. 4. The inhibition of HDAC3 abolishes brain metastasis of soft-primed tumor cells in vivo. (**A**) Schematic of intervention trials. (**B**) Bioluminescence imaging of tumor metastasis at days 0 and 28 after intracardiac injection of soft-primed cells. The mice were treated with or without RGFP966 as shown in (A). (**C**) Kaplan-Meier analysis of brain metastasis–free survival in (B). $n = 12$. (**D**) Quantification of the photon flux in the brain area in (B). $n = 12$. (**E**) Quantification of the photon flux in the brain area and the rest of body at day 28 in (B). $n = 12$. (**F**) Representative immunofluorescence images of Ki-67 staining of coronal brain sections in (B). Tumor cells were labeled with green fluorescent protein (GFP). Scale bar, 1 mm. (**G**) Quantification of lesion size of brain metastases in (F). $n = 12$. (**H**) Quantitation of lesion number of brain metastases in (F). $n = 12$. Log-rank test in (C). Kruskal-Wallis test in [(D), (E), and (G)]. One-way ANOVA with Dunnett's test in (H). $^*P < 0.05$, $^{**}P < 0.01$, and $^{****}P < 0.0001$. Data presented as the means ± SEM.

soft matrices (Fig. 5, B to E, and fig. S14A). Further, this treatment inhibited brain metastasis in vivo (fig. S16, A to C). Narci had no effects on HDAC3 activity or brain colonization but suppressed BBB transmigration and proliferation on soft matrices. In contrast, transient activation of actin cytoskeleton and Rho activity on TCP had no suppressive effects on brain metastasis genes, BBB transmigration, brain colonization, or cell proliferation (fig. S14, B to E). On the other hand, persistent not transient disruption of actin cytoskeleton in parental cells on TCP elevated HDAC3 activity and promoted the brain metastatic functions (Fig. 6, F to J, and fig. S14F). However, the inhibition of ROCK had minimal effects. These results suggest that the repressed mechanotransduction is required for niche softness-induced brain metastasis and that disruption of actin cytoskeleton is sufficient to induce the acquisition of brain metastatic ability in stiff niches.

Low force from soft niches is transmitted through cytoskeleton into nucleus via the linker of nucleoskeleton and cytoskeleton (LINC) complex (*54*), which may influence HDAC3 activity. To explore the roles of nuclear mechanosensing, Nesprin plasmids with dominant-negative Klarsicht/ANC-1/Syne-1 homology (DN-KASH) domain were used to impair the force transmission into the nucleus (*55*). The persistent expression of DN-KASH in parental cells up-regulated brain metastasis genes and HDAC3 activity but attenuated BBB transmigration ability (fig. S15, A, B, and D to F), which may be due to the essential roles of intact LINC complex in motility within confined space (*56*). This treatment had no significant effects on the brain colonization ability (fig. S15G). In comparison, the transient expression of DN-KASH in tumor cells on TCP down-regulated brain metastasis genes (fig. S15C). These results indicate that robust disruption of nuclear mechanosensing is insufficient for tumor cells to acquire brain metastatic ability. We further assessed whether niche softness-induced brain metastatic phenotype depended on nuclear mechanosensing. Parental tumor cells with DN-KASH were persistently primed in soft niches with Jas treatment (Fig. 5K). Jas treatment decreased HDAC3 activity and brain metastatic features (Fig. 5, A to E), which were abolished by DN-KASH. In particular, there was no difference in HDAC3 activity, brain metastasis genes, BBB transmigration, brain colonization ability, or proliferation on soft matrices (Fig. 5, L to O, and fig. S15H). Further, the inhibition of Nesprin-mediated nuclear mechanosensing diminished the effects of Jas treatment on niche softness-induced brain metastasis in vivo (fig. S16, D to F). These results suggest the nuclear mechanosensing mediates soft-primed brain metastasis.

Tumor cells residing in local soft niches of orthotopic xenografts are brain metastatic.

We have demonstrated that soft microenvironments that mimic local soft niches within primary tumors can induce the acquisition of brain metastatic ability in vitro, which is yet to be validated in vivo. We next examined whether tumor cells residing in local soft niches of tumor xenografts exhibited brain metastatic tropism. To tackle this question, we developed a niche softness biosensor (fig. S17A), in which the promoter of a softness-sensitive gene drove mCherry expression in a lentiviral vector. The RNA-seq analysis of soft-/stiff-primed breast cancer cells from both current and previous studies (GSE1278887) (*25*) screened *NDRG1*, *PPL*, *KLRC2*, and *BMF* as candidate genes that were highly up-regulated in soft niches, while no target genes were

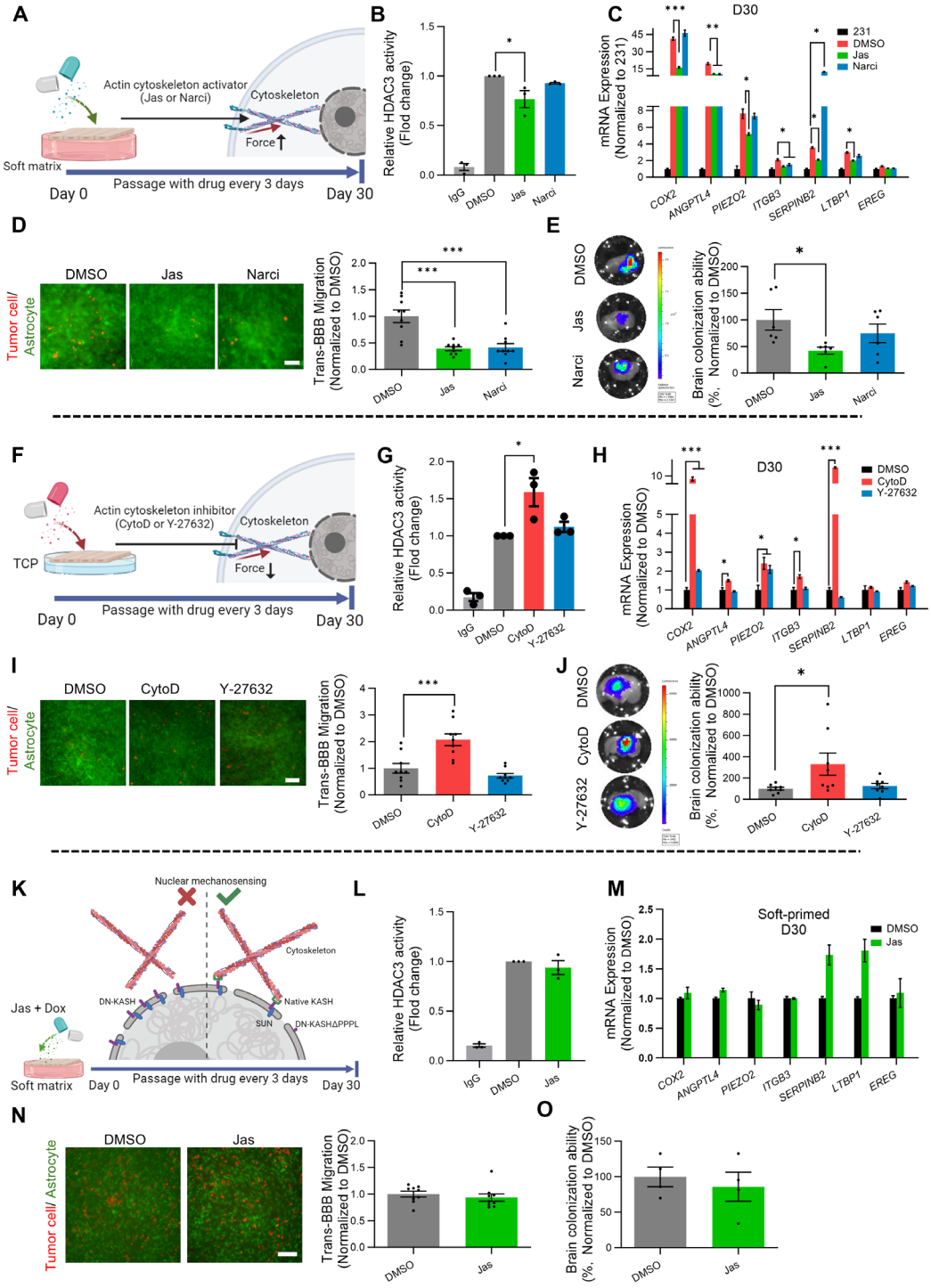

Fig. 5. The repressed mechanotransduction in soft niches promotes HDAC3-mediated brain metastasis. (**A**) Schematic of actomyosin intervention in tumor cells during soft priming. A total of 231 cells were cultured on soft gels in the presence of vehicle, 100 nM Jas, or 10 nm Narci for 30 days. (**B** to **E**) HDAC3 activity measurement (B), RT-qPCR analysis of brain metastasis–related genes (C), BBB transmigration assay (D), and brain colonization assay (E) of the treated cells in (A). $n = 3$ (B and C), 9 (D), and 6 (E). Scale bar, 200 μm in (D). (**F**) The schematic of actomyosin intervention in tumor cells on TCP. A total of 231 cells were cultured on TCP in the presence of vehicle, 100 nM cytochalasin D (CytoD), or 2 μm Y-27632 for 30 days. HDAC3 activity measurement (**G**), RT-qPCR analysis of brain metastasis–related genes (**H**), BBB transmigration assay (**I**), and brain colonization assay (**J**) of the treated cells in (F). $n = 3$ (G and H), 9 (I), and 8 (J). Scale bar, 200 μm in (I). (**K**) Schematic of cytoskeleton and LINC complex intervention in tumor cells during soft priming. A total of 231 cells were transfected with dominant-negative Klarsicht/ANC-1/Syne-1 homology (DN-KASH) plasmids and cultured on 0.6 kPa of PA gels in the presence of vehicle or 100 nM Jas for 30 days. HDAC3 activity measurement (**L**), RT-qPCR analysis of brain metastasis–related genes (**M**), BBB transmigration assay (**N**), and brain colonization assay (**O**) of the treated cells in (K). $n = 3$ (L) and (M), 9 (N), and 4 (O). Scale bar, 200 μm in (N). One-way ANOVA with Dunnett test in [(B) to (E)], [(G) to (J)], and (L). Two-tailed unpaired *t* test in [(M) to (O)]. $^{*}P < 0.05$, $^{**}P < 0.01$, and $^{****}P < 0.0001$. Data presented as the means ± SEM.

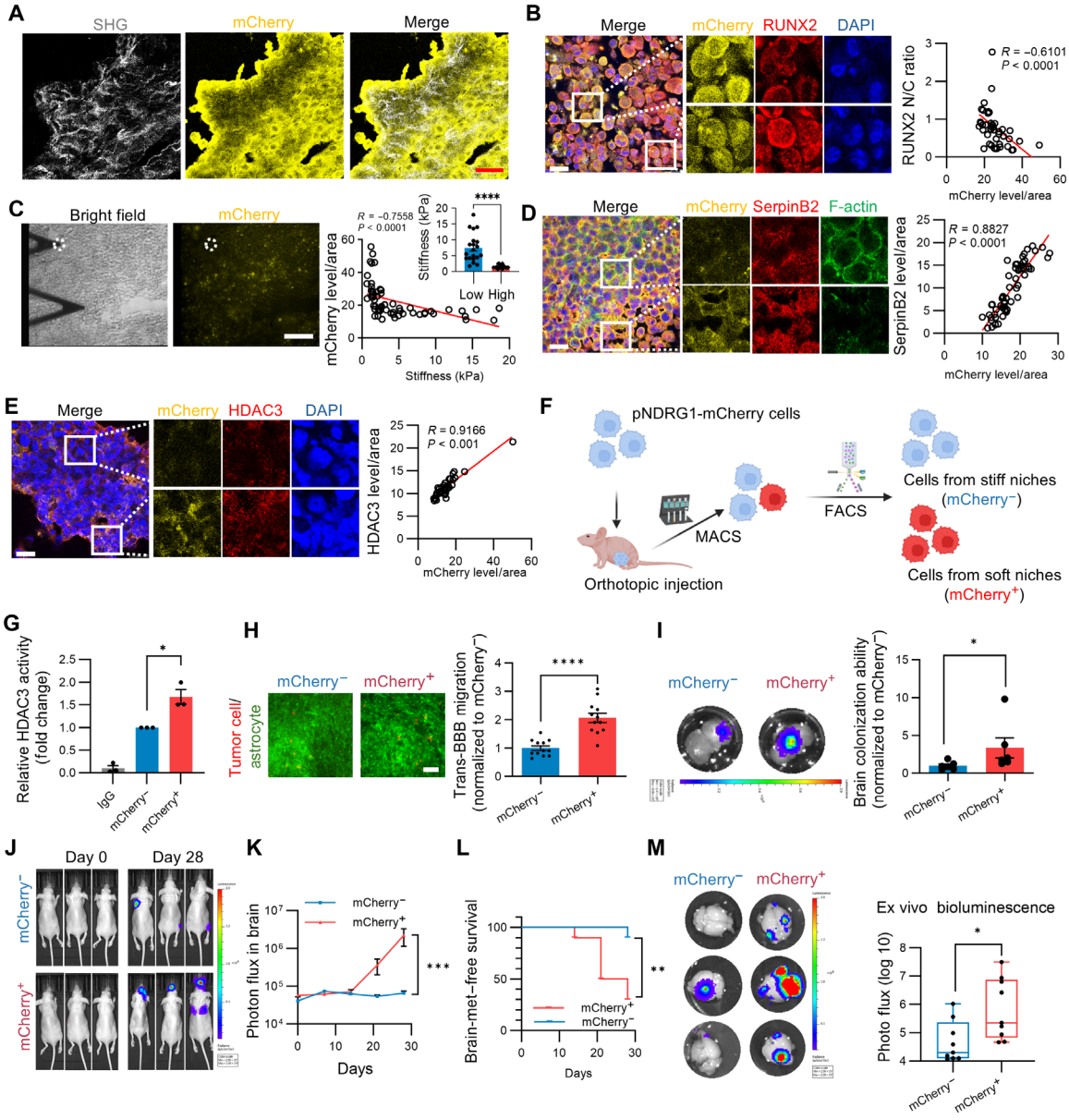

Fig. 6. Tumor cells residing in local soft niches of orthotopic xenografts are brain metastatic. Cryostat sections were derived from pNDRG1-mCherry-TGL-SCP orthotopic xenografts. (**A**) Multiphoton imaging of second harmonic generation (SHG) signal and mCherry in cryostat sections. Scale bar, 25 μm. (**B**) RUNX2 N/C ratio and mCherry level in cryostat sections. Scale bar, 25 μm. The relationship between the mCherry level and RUNX2 N/C ratio was evaluated. $n = 43$. (**C**) Stiffness of local regions with different levels of mCherry in cryostat sections. White dashed line represents the detection area. Scale bar, 100 μm. The relationship between niche stiffness and mCherry level was evaluated. $n = 60$. Insert: The comparison of tissue stiffness between the regions with the top and bottom one-third mCherry signal. $n = 20$. The levels of SERPIN B2 (**D**), HDAC3 (**E**), and mCherry in cryostat sections. Scale bars, 25 μm. The relationship between the mCherry level and SerpinB2 or HDAC3 level was evaluated. $n = 59$ (SerpinB2) and 41 (HDAC3). (**F**) Workflow for isolating tumor cells from soft (mCherry$^+$) and stiff (mCherry$^-$) niches of orthotopic xenografts. HDAC3 activity (**G**), BBB transmigration (**H**), and bran colonization ability (**I**) of mCherry$^{+/-}$ cells. $n = 3$ in (G), 12 (H), and 6 (I). Scale bar, 200 μm. (**J**) Bioluminescence imaging of tumor metastasis at day 0 and 28 after intracardiac injection of mCherry$^{+/-}$ cells. (**K**) Quantification of the bioluminescence in the brain in (J). $n = 10$. (**L**) Brain metastasis–free survival in (J). $n = 10$. (**M**) Bioluminescence imaging of brain tissues ex vivo and quantification. $n = 9$. Spearman's correlation analysis in [(B) to (E)]. Two-tailed unpaired *t* test in (C). One-way ANOVA with Dunnett's test in (G). Two-tailed unpaired *t* test in (H). Mann-Whitney test in [(I), (K), and (M)]. Log-rank test in (L). *$P < 0.05$, **$P < 0.01$, ***$P < 0.001$, and ****$P < 0.0001$. Data presented as the means ± SEM.

identified in stiff niches (fig. S17, B to D). The transcriptional dependency of these genes on niche softness was further confirmed (fig. S17E). We chose *NDRG1* and its associated promoter to construct the pNDRG1-mCherry biosensor due to both its expression level and the monotonic response to stiffness gradient (fig. S17, D and E). Parental cells stably transfected with this softness biosensor expressed higher mCherry in soft than stiff niches (fig. S17F). Within the developed orthotopic tumor xenografts, the mCherry signal was mainly found in the regions with low fibrillar collagen (Fig. 6A). RUNX family transcription factor 2 (RUNX2) is a transcription factor that is typically translocated into nucleus in response to high rigidity (*25*). The nuclear/cytoplasmic ratio of RUNX2 was negatively associated with the

mCherry signal in the xenografts (Fig. 6B). These findings suggest that this biosensor is responsive to niche softness. We further measured the stiffness of the tumor regions with varying levels of mCherry fluorescence. The results showed a negative association between niche stiffness and mCherry signal (Fig. 6C). In particular, local niches with high level of mCherry fluorescence within tumor xenografts were much softer than the regions with low fluorescence signal. Further, the level of F-actin negatively correlated with the mCherry signal (Fig. 6D). Collectively, all these results demonstrate the effectiveness of the developed biosensor to report local niche softness in situ within tumor xenografts.

Further, we explored the association between local niche softness and brain metastatic potential. The integration of this biosensor did not disturb the up-regulation of brain metastasis genes after priming in soft niches (fig. S17G). For pNDRG1-mCherry cells cultured on TCP, the sorted mCherry^{high} cells (10% of the brightest) exhibited even lower SerpinB2 than mCherry^{low} cells (fig. S17H). The distribution of RUNX2 was not correlated with mCherry level, and there was no notable difference in the nuclear/cytoplasmic ratio of RUNX2 between mCherry^{high} and mCherry^{low} cells (fig. S17I). These findings suggest that the developed biosensor may not influence organotropism independent of local niche softness effect. In tumor xenografts, the distributions of SerpinB2 and HDAC3 were significantly correlated with mCherry signal (Fig. 6, D and E), suggesting the association between niche softness and brain metastasis. We further isolated mCherry$^{+/-}$ cells from the developed tumor xenografts, which represented tumor cells residing in local soft and stiff niches (Fig. 6F). mCherry^{+} cells exhibited lower level of RUNX2 nuclear localization and higher levels of SerpinB2 and HDAC3 activity compared to mCherry^{-} cells (Fig. 6G and fig. S18, A and B). mCherry^{+} cells showed advantages in BBB transmigration, brain colonization, and proliferation in the soft microenvironment in vitro (Fig. 6, H and I, and fig. S18C). After intracardiac inoculation, the mCherry^{+} subpopulation exhibited superior potential in initiating the incidence of brain metastasis and promoting the growth of brain metastases compared to mCherry^{-} cells (Fig. 6, J to L). These findings were further supported through *ex vivo* bioluminescence imaging of the harvested brains (Fig. 6M). In summary, these findings demonstrate that local soft niches within tumor xenografts promote brain metastatic tropism of the residing tumor cells.

Niche softness-induced brain metastasis is clinically relevant

Our in vitro and in vivo results have demonstrated that niche softness induces breast cancer brain metastasis. To further explore the clinical relevance of this study, RNA expression profiles of patients with breast cancer from The Cancer Genome Atlas (TCGA) were used to determine whether the expressions of BrM gene signature were correlated with niche softness. The gene set enrichment analysis (GSEA) analysis showed that BrM gene signature was enriched in the primary tumors of breast cancer patients with high NDRG1 level, while BoM gene signature was not enriched in either NDRG1 high or low groups (Fig. 7, A and B). The expression of NDRG1 was positively correlated with BrM but not BoM gene signature (Fig. 7, C and D). Furthermore, NDRG1, PPL, KLRC2, and BMF—which were highly upregulated in soft niches (fig. S17, B to D)—were used as soft score representing soft niches. Previous studies have shown that the gene signatures associated with YAP/TAZ activation are significantly overrepresented in the high-stiffness regulated gene set (*57*). Because no specific target genes were identified in stiff niches (fig. S17, B to D), five downstream genes of YAP (*CTGF*, *CYR61*, *ANKRD1*, *AREG*, and *AXL*) were chosen as stiff score representing stiff niches. Consistent with previous results, soft/stiff gene signature was positively correlated with BrM/BoM gene signature (Fig. 7, E and F). To further dissect the heterogeneity of local niche mechanics and assess the relationship with brain metastasis, we analyzed single-cell RNA-seq dataset of human breast cancer. Single-cell transcriptomes were juxtaposed in uniform manifold approximation and projection (UMAP) space to identify distinct clusters (Fig. 7G). The malignant cell cluster with high NDRG1 expression, high soft score, and low stiff score was identified to originate from local soft niches. Notably, HDAC3 expression and BrM gene signature, but not BoM gene signature, were prominent in such cluster from soft niches (Fig. 7H). To gain insight into the association between spatial stiffness distribution and brain metastatic feature, we analyzed the spatial transcriptomics dataset of human breast cancer (Fig. 7I). We examined the level of NDRG1 expression, soft/stiff score, HDAC3 expression, and BrM/BoM gene signature in each location. The regions with high NDRG1 level also exhibited high soft score, high HDAC3 level, and high BrM gene signature. As expected, the regions with high soft score complemented the regions with high stiff score. Intriguingly, stiff score showed strong positive correlation with BoM gene signature (Fig. 7J). In summary, these results conclude that brain metastasis gene signature and HDAC3 are enriched in local soft niches of human breast cancer biopsies, highlighting the clinical relevance of our study.

DISCUSSION

Tumor cells do not randomly but preferentially disseminate to specific organs for metastatic colonization, which is driven by various biochemical factors, including intrinsic genetic mutation and the microenvironment (*1*) (e.g., specific mutations, organ-specific niches, metabolic reprogramming, and premetastatic niche formation). The essential mechanisms and the acquisition of organotropic potential at specific metastatic steps profoundly determine the development of targeted therapeutic strategies. This study presents compelling evidence to demonstrate that in vitro mechanical priming of tumor cells in soft niches that mimic local soft regions of primary tumor xenografts can promote brain metastasis, which is further supported by the finding that tumor cells isolated from local soft niches of xenografts in vivo exhibit brain metastatic potential. Both results discover the regulatory roles of local niche softness within primary tumor microenvironment in potentiating brain metastasis, highlighting the significance of primary tumor tissue mechanics in metastatic organotropism. It is important to further validate the impact of local soft niches on organotropism in vivo in the patient-derived xenograft model that is closely related to clinical samples (*58*). However, this endeavor remains challenging because there are no methods/tools currently available to faithfully track cells from soft niches in vivo.

Our findings indicate that in addition to the importance of stromal cells and different molecules, the mechanical heterogeneity of local niches distributed in different spatial locations of primary lesions activates distinct signaling pathways via mechanotransduction, which facilitate the preferential dissemination of residing tumor cells to different specific secondary sites. Therefore, this study unveils a previously unappreciated mechanical mechanism underlying metastatic organotropism, particularly brain metastasis, but does not exclude the significance of other factors, such as biochemical signaling, in the

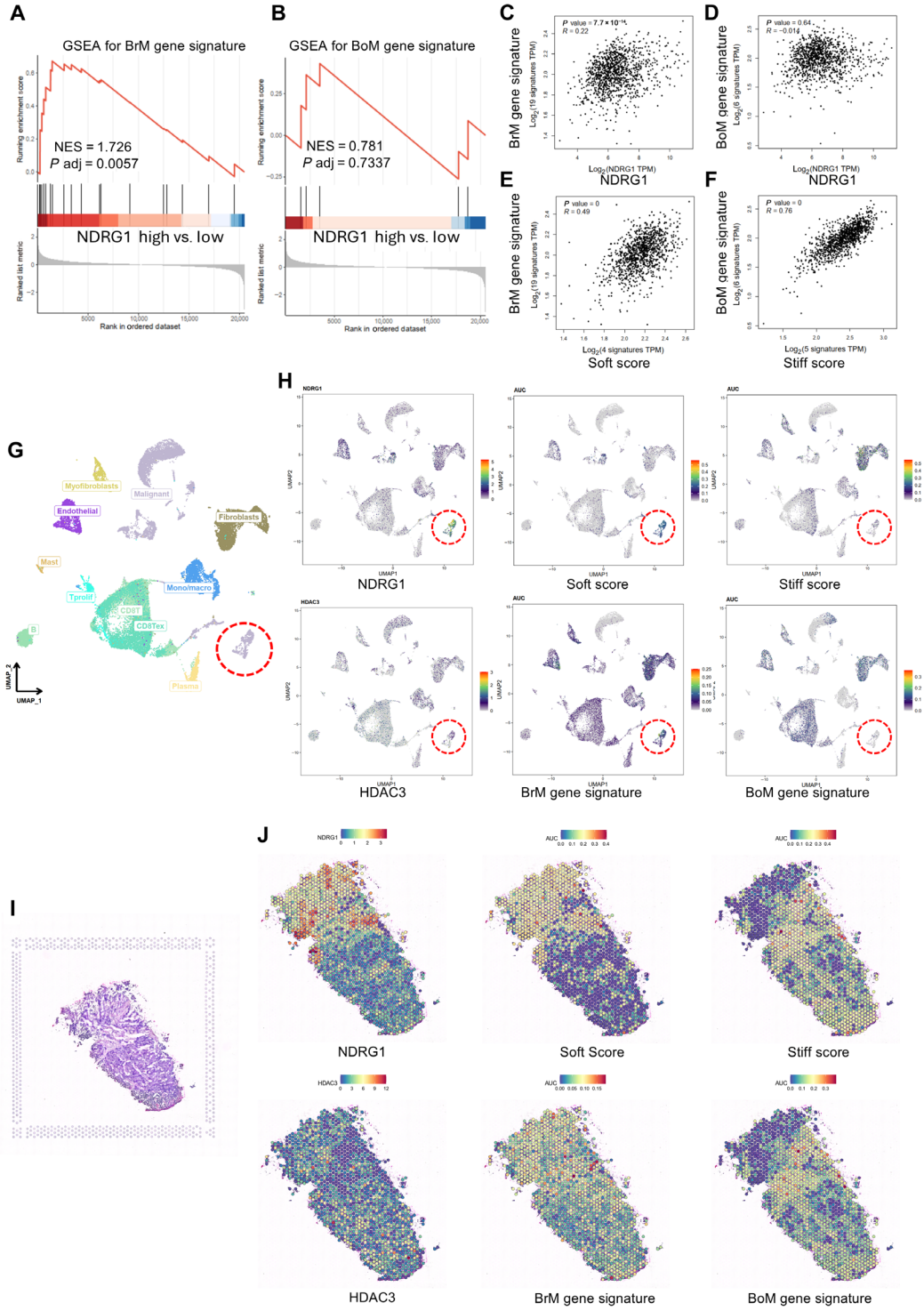

Fig. 7. Niche softness-induced brain metastasis via HDAC3 is clinically relevant in patients with breast cancer. GSEA enrichment plots for BrM (**A**) and BoM (**B**) gene signature in NDRG1 high expression group (top 30%) compared to low expression group (bottom 30%) of patient samples (TCGA-BRCA). Scatterplot showing the correlation between NDRG1 and BrM (**C**) and BoM (**D**) gene signature in patients with breast cancer in TCGA-BRCA. $n = 1085$. (**E**) Scatterplot showing the correlation between soft score and BrM gene signature in patients with breast cancer in TCGA-BRCA ($n = 1085$). (**F**) Scatterplot showing the correlation between stiff score and BoM gene signature in patients with breast cancer in TCGA-BRCA. $n = 1085$. (**G**) Uniform manifold approximation and projection (UMAP) visualization of scRNA-seq datasets obtained from the samples of patients with breast cancer in EMTAB8107. Clusters were annotated for their cell types. (**H**) Visualization of normalized expression levels of NDRG1, HDAC3, soft/stiff score, and BrM/BoM gene signature. Red dashed line indicated tumor cell cluster originating from soft niches. (**I**) Complete H&E images of tissue region analyzed for the breast tumor sample GSE210616_GSM6433585. (**J**) AUCell signature scores of NDRG1, HDAC3, soft/stiff score, and BrM/BoM gene signature. Signature scores were computed using the AUCell method. AUC, area under the curve.

propensity of metastasis to target organs. Instead, these discoveries expand our current understanding and support the proposition that mechanical cues may play as important roles as biochemical factors in metastatic organotropism. In the complex tumor microenvironment, these biochemical and mechanical signaling could function independently and/or synergistically to facilitate organ-specific metastasis.

Recent decades have witnessed the rapid accumulation of evidence showing the remarkable remodeling of primary tumor microenvironment (*12*, *42*), including the excessive deposition of ECM proteins, leading to the overall stiffening of tumor tissue as a whole in multiple types of cancer (*12*). Many previous studies have demonstrated the importance of the stiffened primary tumor in different metastatic steps (*42*), such as malignant transformation (*59*), migration and invasion (*14*), intravasation (*15*), the interaction of tumor cells with endothelium (*16*), and overt metastasis (*60*). Most of these studies have assumed that the entire primary tumor becomes stiffened uniformly or only focused on the roles of stiffened niches within primary tumors. However, significant intratumoral heterogeneity, a hallmark of cancer, could lead to substantial variations of local niche stiffness within the primary tumor microenvironment (*29*). Yet, the influence of primary tumor mechanical heterogeneity on metastasis remains poorly investigated. In this study, we propose that the mechanically heterogenous primary tumor niches may drive the emergence of organ-specific metastatic subpopulation through both clonal selection and phenotypic reprogramming. In particular, mechanical priming in soft niches confers brain metastatic ability, and cancer cells originating from local soft niches of primary tumors exhibit brain metastatic traits. Besides, breast cancer cells after priming in stiff niches may acquire bone metastatic potential in vivo, which may be attributed to the osteolytic phenotype induced by niche stiffness, as reported in previous studies (*24*, *25*). Therefore, our results unambiguously support an unrecognized notion that the heterogeneous primary tumor stroma mechanics could be one determinant of metastatic tropism. Further, the recognition of overall tissue stiffening in promoting tumor metastasis has prompted the idea of targeting primary tumor stiffness and the mediated mechanotransduction signaling as a promising strategy for cancer therapy, such as beta-aminopropionitrile for lysyl oxidase (*61*). However, our findings warrant a revisit into the potential risks associated with disruption of tumor tissue mechanics. Instead, the complex mechanical heterogeneity should be taken into consideration when developing new mechanotherapeutics.

We have shown that soft priming is sufficient to trigger the up-regulation of neuron-related pathways and induce transcriptomic reprogramming of tumor cells with the signature similar to brain cell types, which are favorable to brain metastasis. This finding is in line with previous studies: Brain metastatic tumor cells undergo adaptive transcriptomic transformation to acquire the characteristics similar to nerve cells, a process termed neuronal mimicry (*31*); tumor cells from brain metastases exhibit GABAergic features, providing an alternative mechanism of malignant adaptation to fuel metastatic colonization in the brain (*30*); the neural glutamate receptor NMDAR promotes brain metastasis of breast tumor cells (*62*); the gene expression patterns resembling brain cells may already exist in primary breast tumors of patients who later develop brain metastases, indicating that tumor cells may develop nerve-like characteristics in the primary tumor for the subsequent brain metastasis (*63*). In addition, soft matrix–mediated reduced mechanotransduction facilitates neuronal differentiation of stem cells and neuronal reprogramming of adult cells (*64*, *65*). Nevertheless, rigorous studies are needed to investigate the roles of primary tumor mechanical heterogeneity in neuronal mimicry and the molecular mechanisms.

This study has demonstrated that soft niches facilitate the acquisition of brain metastatic ability through the repressed mechanotransduction-mediated HDAC3 activation (Fig. 8). Pharmacologic inhibition of HDAC3 not only abolishes niche softness-induced brain metastatic phenotype but also prevents the outgrowth of brain micrometastases, which may be instructive for the suppression of metastatic colonization in brain, because organtropic cells probably have already disseminated to target organs when patients are first diagnosed. Aberrant HDAC3 expression is highly related to the prognosis of patients with brain metastases (*66*). HDAC inhibitor vorinostat (SAHA) has shown potential in treating brain metastases in breast cancer (*67*). Because HDAC3 affects histone deacetylation, chromatin accessibility (*68*), and the functions of transcription factors (*69*), it is of interest to rigorously investigate whether HDAC3 affects the expressions of brain metastasis-related genes through the epigenetic and/or transcriptional mechanisms in the future. While the molecular mechanisms by which niche softness-mediated mechanotransduction regulates HDAC3 activity require further investigation, multiple nuclear envelope proteins have been reported to modulate HDAC3 activity. For example, Emerin facilitates HDAC3 localization to the nuclear lamina and increases its enzymatic function by binding to HDAC3 (*70*). Lamina-associated polypeptide 2, β-isoform (LAP2β) interacts with HDAC3 to promote its histone deacetylation (*71*). These nuclear envelope proteins may play a role in niche softness-mediated regulation of HDAC3 activity, which warrants further investigation. Collectively, our findings, together with earlier studies, shed light on the significance of HDAC3 in mechanotransduction-induced brain metastasis and the potential of targeting HDAC3 as a promising strategy against brain metastasis.

This study characterizes the mechanical heterogeneity of breast tumor xenografts and finds that mechanical priming in soft niches, mimicking local soft regions in primary tumors, induces neuronal-like

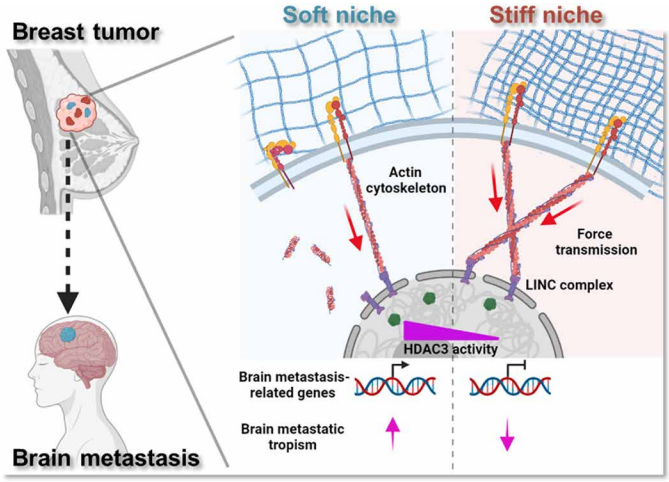

Fig. 8. Summary of niche softness-induced brain metastatic tropism via actin cytoskeleton-LINC complex-HDAC3 axis. The primary tumor microenvironment is mechanically heterogeneous and contains local soft and stiff niches. Persistent priming in soft but not stiff niches represses the actin cytoskeleton-LINC complex-mediated mechanotransduction, which further enhances HDAC3 activity, leading to the up-regulation of brain metastasis–related genes and acquisition of brain metastatic tropism.

transcriptional reprogramming and promotes the acquisition of brain metastatic phenotype. Soft-primed tumor cells preferentially disseminate to brain for the establishment of secondary lesions through enhanced transendothelial migration across BBB and brain colonization. These findings are validated by the results that tumor cells isolated from local soft niches of primary xenografts exhibit brain metastatic potential. Further, soft niches repress mechanotransduction signaling to promote HDAC3 activity. The inhibition of HDAC3 abolishes both niche softness-induced brain metastatic traits and the outgrowth of brain micrometastases. In summary, this study discovers an unrecognized role of primary tumor mechanical heterogeneity in metastatic organotropism, particularly brain metastasis.

MATERIALS AND METHODS

Cell culture

MDA-MB-231 (231) cell line and its brain metastatic derivative, MDA231-BrM2-831 (231-BrM), as well as the bone metastatic derivative, MDA-BoM-1833 (231-BoM), were obtained from Memorial Sloan Kettering Cancer Center. These cell lines were cultured in Dulbecco's modified Eagle's medium (DMEM; HyClone) supplemented with 10% fetal bovine serum (FBS; HyClone) and 1% penicillin/streptomycin (Gibco). The human cerebral microvascular endothelial cell line hCMEC/D3 (FuHeng Biology) was cultured with EndoGRO-MV complete culture media kit (Sigma-Aldrich), which was supplemented with human basic fibroblast growth factor (200 ng/ml; Sigma-Aldrich) and 1% penicillin/streptomycin. The human umbilical vein endothelial cells (HUVECs) and human astrocytes, which were isolated from the cerebral cortex of the human brain, were purchased from American Type Culture Collection (ATCC) and ScienCell, respectively. HUVECs were cultured in Endothelial Cell Medium (ScienCell), and human astrocytes were cultured in Astrocyte Medium (ScienCell). Human embryonic kidney–293T cell line was a gift from R. Yechun (The Hong Kong Polytechnic University) and was cultured in DMEM supplemented with 10% FBS and 1% penicillin/streptomycin. 4T1 cells, which were purchased from ATCC, were cultured in RPMI 1640 medium (Gibco) with 10% FBS and 1% penicillin/streptomycin. All cell lines were cultured in a 5% CO_2 incubator at 37°C.

Synthesis of PA hydrogels (PA gels)

The hydrogels were prepared according to an established protocol described previously (*72*): Circular coverslips were treated with aminosilane (Aladdin) and glutaraldehyde (Aladdin), while glass slides were treated with chloro-silane in accordance with the instructions. Acrylamide [AA; 40% (w/v)] and bis-acrylamide [BA; 2% (w/v)] were then mixed in distilled water to obtain the desired concentrations. Hydrogel formulations were as follows

7.5% (v/v) AA + 3% (v/v) BA + 89.5% (v/v) H2O (0.6 kPa);

25% (v/v) AA + 15% (v/v) BA + 60% (v/v) H_2O (35 kPa).

The 1:100 total volume of 10% ammonium persulfate (Sigma-Aldrich) and 1:1000 total volume of tetramethylethylenediamine (Sigma-Aldrich) were quickly added and mixed with the gel solution. Subsequently, 240 μl (for six-well plates) of the gel solution was pipetted onto the chloro-silanated glass slide and covered with an aminosilanated coverslip. After polymerization, the hydrogel was immersed in phosphate-buffered saline (PBS; Hyclone) and stored at 4°C. The gel surface was coated with Sulfosuccinimidyl-6-(4′-azido-2′-nitrophenylamino) hexanoate (Sigma-Aldrich) under 365-nm ultraviolet (UV) light. After washing with PBS three times, the gel was coated with either rat-tail collagen type I (0.2 mg/ml; Sigma-Aldrich) or human plasma fibronectin (10 μg/ml; Sigma-Aldrich) and incubated at 4°C overnight. The gel was sterilized by UV light for 30 min in a cell culture cabinet and incubated with 1 ml of full medium for at least 30 min before use.

Quantitative RT-PCR analysis

Total mRNA was extracted using the E.Z.N.A. Total RNA Kit (Omega) following the manufacturer's recommended protocol. RevertAid First Strand cDNA Synthesis Kit (Thermo Fisher Scientific) was used to synthesize cDNA from the extracted total RNA. The primers for quantitative reverse transcription polymerase chain reaction (RT-PCR) were designed on the basis of sequences from the National Center for Biotechnology Information (NCBI) database and listed in table S1. The Forget-Me-Not EvaGreen qPCR Master Mix with Rox (Biotium) and CFX96 Real-Time System (Bio-Rad) were used to perform quantitative RT-PCR. The relative gene expression was calculated using the 2-ΔΔ*C*T method and normalized to the expression of the human glyceraldehyde-3-phosphate dehydrogenase (GAPDH).

RNA sequencing

Total RNAs were extracted from each sample using the RNeasy Mini Kit (QIAGEN). The sample quality—such as quantitation, integrity, and purity—was assessed using Agilent 5400 to ensure that the samples met the library construction requirements.

mRNAs were purified from total RNA using poly-T oligo-attached magnetic beads. After fragmentation, first-strand cDNA was synthesized using random hexamer primers, followed by second-strand cDNA synthesis. The quality and quantity of libraries were assessed using Qubit and real-time PCR, and the bioanalyzer was used to determine the size distribution. Quantified libraries were pooled and sequenced on Illumina platforms based on effective library concentration and data amount. The index-coded samples were clustered according to the manufacturer's instructions, and paired-end reads were generated on the NovaSeq PE150 platform by Novogene. All downstream analyses were based on clean, high-quality data provided by Novogene. FPKM, expected number of fragments per kilobase of transcript sequence per millions base pairs sequenced, was calculated on the basis of gene length and read count, and differential expression analysis was performed using the DESeq2R package (1.20.0). Genes with an adjusted *P* value (P_{adj}) ≤ 0.05 found by DESeq2 and $|\log_2(\text{fold change})| \geq 1$ were identified as differentially expressed. In addition, RNA-seq data of SUM159 breast cancer cells cultured on 0.5 and 8 kPa of substrates for 14 days were acquired from GSE127887 in the Gene Expression Omnibus (GEO) database (www.ncbi.nlm.nih.gov/geo/).

In bioinformatic analysis of RNA-seq data, enriched terms and pathways in gene ontology (GO), DisGeNET, and PaGenBase databases were analyzed using over-representation analysis (ORA) by Metascape (https://metascape.org/gp/index.html#/main/step1). The threshold for significant levels was set to $P_{adj} \leq 0.05$ for terms and pathways. GSEA was performed using easyGSEA (https://tau.cmmt.ubc.ca/eVITTA/easyGSEA/) with default parameters (minimum gene set size: 15, maximum gene set size: 200, and the number of permutations: 1000). The threshold for significant levels was set to $P_{adj} < 0.25$ and normalized enrichment score (NES) > 1 for terms and pathways. The STRING database (version 10) and the ENCODE ChIP-seq

database were used to analyze the generic protein-protein interactions network and gene regulatory network, respectively. The networks were visualized using NetworkAnalyst (www.networkanalyst.ca/). ImageGP (https://www.bic.ac.cn/ImageGP/) was used to generate volcano plots, bubble plots, and heatmaps.

Bioinformatics analysis

TCGA dataset analysis

The data were obtained from TCGA (www.cancer.gov/tcga) breast invasive carcinoma (TCGA-BRCA) containing 1085 individual primary tumor samples. On the basis of the 30% gene expression values, the samples are stratified into high and low expression groups. The limma package is used to conduct differential analysis, yielding the $\log_2$ fold change ($\log_2$FC) for each gene, which are subsequently sorted based on $\log_2$FC values. Subsequently, the clusterProfiler package conducts GSEA using the BrM/BoM gene signature. The enrichment fraction (ES) of gene sets is computed, followed by significance testing and multiple hypothesis testing for the ES values of the gene sets. The Cor.test function was used to calculate the Pearson correlation of genes and/or gene sets.

scRNA-seq and spatial transcriptomics analysis

Breast cancer single-cell RNA sequencing (scRNA-seq) data (EMTAB8107) were downloaded from the TISCH2 database. Data were processed by Sparkle database (https://grswsci.top/), including quality control, clustering, cell-type annotation, malignant cell classification, area under the curve score calculation of gene sets, and visualization. Spatial transcriptomics data were downloaded from GEO database (GSE210616_GSM6433585) and analyzed by Sparkle database and SpatialTME (www.spatialtme.yelab.site/). In detail, the cellular composition was deconvoluted using Cottrazm package (*73*). Sparkle database was used to integrate 10x Visium sequencing data in SpatialTME database and visualize spatial maps.

In vitro circulation system

An in vitro circulation system, consisting of a peristaltic pump (Harvard Instruments, P-230), a 10-ml syringe and a 1.5-m-long silicone microtube with a diameter of 0.51 mm, was used to generate fluid shear force (*74*, *75*). Wall shear stress was modulated by adjusting the flow rate, following Poiseuille's law: $\tau = 4\mu Q/(\pi R^3)$, where Q represents the flow rate, $\mu = 0.01$ dyne/cm^2 is the dynamic viscosity of the cell culture media, and $R = 0.255$ mm is the radius of the tube. All components of the system were exposed to UV for 15 min. The tube and syringe were sterilized with 75% ethanol for 5 min, washed with PBS for 5 min, and then pretreated with 1% bovine serum albumin (BSA; VWR Life Science) in PBS for 5 min to prevent unspecific adhesion of suspended cells to the channel wall. Subsequently, 4×10^5 of suspended cells were plated into the circulation device and exposed to a wall shear stress of 20 dyne/cm^2 for 6 or 12 hours at 37°C in a 5% CO_2 incubator.

MTS assay

Initially, 100 μl of cell suspension was obtained from the in vitro circulation system and added into a clear 96-well cell culture plate. The plate was then subjected to a 12-hour incubation period. Following this, 20 μl of a working solution (5 mg/ml) from CellTiter 96 aqueous One Solution Reagent (Promega) was added into each well, and the plate was incubated at 37°C. After 4 hours, the absorbance of the cell solution was measured at 490 nm using a LEDETECT 96 microplate reader (Labexim Products).

Cell adhesion assay

Endothelial cells were cultured until confluency in six-well cell culture plates, and tumor cells were labeled with CellTracker Green CMFDA Dye (Invitrogen) or PKH26 red fluorescent cell linker kit (Sigma-Aldrich). Before seeding tumor cells, the endothelial monolayers were washed twice with 0.5% BSA in PBS. Next, 1 ml of 1×10^5 suspended tumor cells was added to each well and allowed to attach for either 15 or 30 min. The medium was then removed, and the plates were washed with PBS three times for 5 min each. The adhered cancer cells were quantified using an inverted fluorescent microscope (Nikon).

To perform the substrate adhesion assay, 1×10^5 of suspended tumor cells were added to the corresponding functionalized surface of PA gels and incubated for either 15 or 30 min in the cell incubator. The wells were then rinsed three times with PBS for 5 min each, and adhered tumor cells were counted under an inverted microscope.

In vitro BBB transmigration assay

The Transwell insert with a pore size of 3 μm (Corning, #3415) was first treated with poly-L-lysine (1 μg/ml; Sigma-Aldrich) overnight and washed with PBS four times before being treated with 0.2% gelatin (Sigma-Aldrich) for 30 min. The insert was then inverted and placed in a 12-well plate, and 1×10^5 of primary human astrocytes were resuspended in 30 μl of culture medium and plated on the membrane surface. The astrocytes were fed with media every 15 min for 5 hours, and then, the insert was flipped and placed in 24-well plates. Next, 5×10^4 of hCMEC/D3 cells were added to the upper chamber of the insert, and the plate was placed in the incubator for 3 days without any perturbation before use. To label the cancer cells, 1×10^5 of cells were collected and incubated with CellTracker Deep Red Dye (Invitrogen) according to the manufacturer's instructions. After being labeled with the cell tracker, cells were resuspended with serum-free medium and added to the upper chamber of the Transwell insert. After incubation for 48 hours, noninvading cells were removed. The chamber was washed with PBS and fixed with 4% paraformaldehyde (PFA) and then stained with 4′,6-diamidino-2-phenylindole (DAPI). Immunofluorescence images were taken in multiple fields from three to six inserts per experiment, and the number of transmigrated cells was counted.

Cell morphology analysis

After treatment, cells were seeded onto their corresponding substrates and incubated for 24 hours. Images were captured using an inverted or fluorescence microscope, from which cell boundaries were identified. The parameters representative of cell morphology—such as area, circularity, and aspect ratio—were analyzed using ImageJ software (NIH).

Western blotting analysis

Total protein samples were extracted from treated cells using radioimmunoprecipitation assay buffer (Thermo Fisher Scientific, # 89901) supplemented with protease inhibitor cocktail (Thermo Fisher Scientific, # 78430) and phosphatase inhibitor cocktail (Thermo Fisher Scientific, # 78420). The proteins were separated using SDS–polyacrylamide gel electrophoresis gel electrophoresis and then transferred to methanol (Aladdin)–prewetted polyvinylidene difluoride (PVDF) membranes (Millipore) using Trans-Blot Turbo (Bio-Rad). Subsequently, the PVDF membranes were blocked with Beyotime blocking buffer (#P0252)

for 1 hour to prevent nonspecific binding. Primary antibodies—including COX2 (1:1000; Abcam, ab188183), HDAC3 (1:5000; Abcam, # ab32369), and GAPDH (1:2000; Abcam, # ab8245)—were diluted in blocking buffer and incubated with the PVDF membranes for 12 hours at 4°C. The membranes were washed thrice with TBST (5 min each time) before being incubated with the appropriate horseradish peroxidase (HRP)–conjugated secondary antibody (diluted at 1:2000 in blocking buffer) for 1 hour at room temperature. The following secondary antibodies were used: goat anti-rabbit antibody conjugated to HRP (1:2000; Bio-Rad, #1662408EDU) and goat anti-mouse igg (H+L)-HRP conjugate (1:2000; Bio-Rad, #1706516). The membranes were washed thrice with TBST (5 min each time) following the secondary antibody incubation, then incubated with Clarity Western ECL Substrate (Bio-Rad, #1705061), and imaged by a ChemiDoc imaging system (Bio-Rad). The immunoreactive bands were quantified using ImageJ, and their densities were normalized to the density of GAPDH.

ELISA for PGE2

Cancer cells were seeded at a density of 3×10^5 cells per well on tissue culture plates or PA gels with varying stiffness. Following a 24-hour incubation, we collected the supernatants and measured the level of PGE2 using the PGE2 enzyme-linked immunosorbent assay (ELISA) kit (Abcam, #ab133021) according to the manufacturer's protocol. The colorimetric signal of the samples was detected using the LEDETECT 96 microplate reader.

Cell proliferation assay

To assess cell proliferation, we utilized the 5-ethynyl-2′-deoxyuridine (EdU) proliferation kit (Beyotime, #C0078L) as per the manufacturer's instructions. Briefly, cells were incubated in complete culture medium, and EdU stock solution was diluted 500 times to obtain the 2× working reagent. The working reagent was prewarmed to 37°C and added to each well along with an equal amount of complete culture medium. After 2 hours of incubation at 37°C, the cells were collected and treated with 4% PFA followed by permeabilization with 0.3% Triton X-100. The click reaction buffer was then added to stain the cells for 30 min in the dark at room temperature. DAPI solution was used to stain the nuclei of the cells, which were then rinsed with PBS. The percentage of EdU-positive cells was determined by fluorescence microscopy or flow cytometry.

Live/Dead staining assay

The viability of cells was evaluated using the calcein/propidium iodide (PI) live/dead viability assay kit (Beyotime, #C2015L) as per the manufacturer's instructions. Briefly, cells were seeded onto the corresponding matrix and incubated for 24 hours. Calcein AM/PI detection working solution was prepared according to the manufacturer's instructions. After removing the culture medium, 1 ml of calcein AM/PI detection working solution was added to each well of a six-well plate and incubated for 30 min. The fluorescence images of live/dead staining were captured, and the ratio of live/dead cells was calculated by ImageJ.

Wound healing assay

The ibidi Culture-Insert 2 Well (ibidi, # 80209) was used to perform the wound healing assay. Cells were adjusted to a concentration of 3×10^5 cells/ml, and 70 μl of the cell suspension was added to each well of the Culture-Insert 2 well. After incubating cells at 37°C and 5% CO_2 for at least 24 hours, the Culture-Insert 2 well was gently removed using sterile tweezers. The cell layer was washed with PBS to remove cell debris and nonattached cells, and 2 ml of medium with 2% FBS was added. Microscopic images were taken at the indicated time points, and the healing degree was calculated by dividing the healing area at the end time point by the wound area at the start time point. The wound and healing areas were measured using ImageJ.

Transwell invasion assay

Matrigel was polymerized in the upper chamber of a Transwell insert with 8.0-μm pore polycarbonate membrane. Varying concentrations of Matrigel were used to create gels of different rigidities, ranging from 2 to 4 mg/ml. The full-length fibronectin (FN) was added to the gels at a final concentration of 10 mg/ml before polymerization. After the gels were formed, 1×10^5 of cells suspended in serum-free medium were added to the upper chamber, and the lower chamber was filled with 500 μl of full culture medium. After incubation for 48 hours, the cells on the upper side and Matrigel were removed, and the remaining cells on the other side were stained with 0.1% crystal violet solution. The number of invaded cells was counted under a 20× objective, and a minimum of five representative fields were counted for each condition.

Collagen gel invasion assay

Cell suspension (3×10^5 cells/ml) was added to each well of the ibidi Culture-Insert 2 well in a 24-well plate, which produces a scratch after 24 hours of incubation. Type I rat tail collagen of different concentrations (0.5, 1, and 3 mg/ml) was then added to the top of cells after the Culture-Insert 2 well was removed. The pH of the collagen was neutralized using NaOH, and the cell layer was covered with 500 μl of the neutralized collagen solution. After collagen solidification, cell culture medium with 2% FBS was added to the top of the gels, and images were taken to measure the healing degree of the scratches after 24 hours.

Soft agar assay

For the soft agar colony formation assay, a base agar layer was first prepared. Low melting point agarose (Sigma-Aldrich, #39346-81-1) was diluted in 1% agarose with DMEM to make 3% agarose solution. A 2 ml of 1% agarose solution was pipetted into each well of a six-well cell culture plate and allowed to solidify at room temperature for at least 30 min. For the top agar layer containing cells, 0.8% agarose solution was prepared by mixing full cell culture medium, 3% agarose, and FBS in a 6.3:2.7:1 ratio and stored in a 42°C water bath. Cells were resuspended in full culture medium at a concentration of 2.5×10^3 cells/ml and mixed with an equal volume of the 0.8% agarose solution. A total of 2 ml of the cell-agarose mixture was added to each precoated well and incubated at 4 °C for 15 min to allow for solidification. Afterward, 300 μl of full cell culture medium was added to the top of the agar, and the plate was incubated at 37°C with 5% CO_2. A total of 200 μl of full culture medium was added to each well every 3 days. After 28 days of incubation, the plate was stained with 0.5 ml of 0.1% crystal violet (dissolved in 10% ethanol) for 1 hour. Colonies from at least three wells were imaged using a ChemiDoc imaging system and counted using ImageJ software.

AFM measurement

In this study, we used an atomic force microscope (AFM; BioScope Catalyst, Bruker) in combination with an inverted fluorescence microscope (Nikon) equipped with a 20× objective to visualize the probe

and facilitate precise control of tip and sample position. Cells were seeded on PA gels or TCP for 24 hours with a density below 30% confluency before measurement. Cryostats tumor sections were attached to coverslips with poly-L-lysine. We selected silicon cantilevers (MLCT, Bruker) with a spring constant k of 0.02 and 0.03 N/m for the stiffness measurement for cell and tissue sample, respectively. AFM calibration was performed in accordance with the user manual. Specifically, we chose the contact mode and ScanAsyst in Fluid mode to detect cell and tissue stiffness in the medium. Subsequently, we performed laser positioning, AFM positioning, and cantilever calibration in sequence. The force F between the probe and the sample was calculated by the formula $F = k \times \delta$, where k is the spring constant of the cantilever and δ is the indentation, which is equal to the sample height minus the deflection. To obtain Young's modulus E of the sample, we used the Sneddon model to fit force-indentation curves for a pyramidal probe: $F = 2/\pi \times \tan(\alpha) \times E/(1 - \nu^2) \times d^2$, where d is the depth of indentation, α is half of the tip angle, and ν is the Poisson ratio (e.g., 0.5). We set d below 500 nm to avoid cell damage. The perinuclear area was probed to minimize the effect of substrate-induced outliers.

Ultrasound shear-wave elastography

The methods of using B-mode ultrasound and shear wave elastography on orthotopic xenograft were previously described (*76*). Mice were anesthetized at 8 weeks after orthotopic injection. Ultrasound coupling gel (Aquasonic CLEAR, AquasonicGel, MI, USA) was smeared on the skin outside the primary lesion, when tumor margins were then determined by B-mode ultrasound. Tumor stiffness was detected using shear wave elastography imaging with an Aixplorer Scanner (SuperSonic Imagine, France) incorporating a SL22-7 linear array transducer (SuperLinear, SuperSonic Imagine, France).

HA hydrogel fabrication

To synthesize methacrylated hyaluronic acid (MeHA), we prepared a 1 weight % (wt %) solution of sodium hyaluronate in deionized water (DI water). We added methacrylic anhydride (MA) (2 ml per g HA) dropwise at 4°C with stirring and maintained pH at 8.5 through continuous addition of 2 M NaOH solution for approximately 8 h. Subsequently, we further added MA (2 mL per gram HA), maintained pH at 8.5 for approximately 4 hours and then left overnight at 4°C. After dialyzing against NaCl solution and DI water for 2 days, we froze MeHA at −80°C, lyophilized, and stored it at −20°C as powder. For cell encapsulation, we prepared a HA hydrogel solution to a final concentration of 2 wt % MeHA and 0.5% wt lithium phenyl-2,4,6-trimethyl-benzoyl phosphinate photo-initiator in PBS. Cells were harvested and resuspended in full culture medium at 2×10^6 cells/ml. We mixed the HA hydrogel solution with the medium containing cells at a 1:1 ratio and exposed it to 365-nm UV light for 1 min. The polymerized HA gel was then placed on a 96-well culture plate and soaked with full culture medium.

Dot blot assays

Cells were seeded in a six-well plate at a density of 2×10^5 cells per well and allowed to grow for 24 hours. Next, 100 μl of supernatant medium was transferred onto a nitrocellulose membrane with a pore size of 0.45 μm (Millipore) and allowed to adsorb for 1 hour at room temperature. The remaining liquid was aspirated, and the membrane was blocked with 5% dry milk in 0.1% Tween-TBS (TBST) for 1 hour. Subsequently, the membrane was incubated overnight at 4°C with an anti-SERPINB2 antibody (1:500 in blocking solution; Abcam, # 47742). After washing three times with TBST for 5 min, the membrane was incubated with an anti-rabbit HRP-coupled IgG (1:2000 in blocking solution) for 1 hour, followed by repeated washing. Last, the signal was detected using ECL solution (Bio-Rad).

Brain slice assay

Brain slices from the adult mouse brain were prepared following the method previously reported (*77*). Brains were obtained from female BALB/c nude mice aged 6 to 8 weeks and embedded in preheated low-melting agarose at a temperature of 42°C. The agarose-embedded brains were then sectioned into 250 μm slices using a vibratome (Leica, VT1200S). Subsequently, brain slices were transferred to 0.8-μm pore membranes (Millipore), and slice culture medium (DMEM supplemented with Hanks' balanced salt solution, 5% FBS, 1 mM L-glutamine, and 1% penicillin/streptomycin) was supplied. After brain slices were incubated at 37°C with 5% CO_2 for 1 hour, 2 μl of medium containing 3×10^4 tumor cells was added onto each slice and incubated for 48 hours. To assess the colonization of tumor cells on brain slices, brain slices were gently washed with PBS. Then, 1 ml of D-luciferin (300 μg/ml; Abcam) was added into each well to cover the slice, and bioluminescence signals were measured using the IVIS Lumina Series III preclinical in vivo animal imaging system (PerkinElmer).

Animal experiments

In all the animal experiments, we followed the National Institutes of Health's Guide for the Care and Use of Laboratory Animals and obtained approval from the Animal Subjects Ethics Subcommittee of Hong Kong Polytechnic University for all experimental protocols (ethics approval #23-24/671-BME-R-CRF). Throughout the experiments, analgesic buprenorphine was administrated through drinking water to minimize the suffering if signs of pain or discomfort were observed. Animal were terminated humanely after the experiments, which complied with the 5 Freedoms in animal welfare and the 3Rs (Reduction, Replacement, and Refinement) principles.

Cell preparation for animal experiments

Cells were trypsinized and resuspended at 1×10^6 cells/ml for intracardiac injection, 2×10^4 cells/3 μl for intracerebral injection in 1% BSA (IgG-free) in ice-cold PBS, and 1.5×10^6 cells/50 μl mixed with 50 μl of Matrigel on ice for orthotopic injection. The mixture was kept on ice and gently mixed by finger flicking before injection. Experiments were carried out on 6- to 8-week-old female BALB/c nude mice.

Intracardiac injection

Mice were anesthetized by intraperitoneal injection with (8.7 mg of ketamine + 1.3 mg of xylazine)/100 g. The injection site was located in the middle between the sternal notch and the top of the xiphoid process and on the left side of the sternum (anatomical position). A 100 μl of cell suspension was injected with needle upright and inserted into the left ventricle with bright red pulse in the syringe. After injection, pressure was applied lightly at the injection site to reduce bleeding, and the mouse was placed on a heating pad until it was fully conscious. The entire experimental process lasted 28 days for long-term in vivo organotropic metastasis assay, and bioluminescence imaging was conducted every 7 days to monitor the metastatic pattern. For in vivo BBB penetration assay, bioluminescence imaging was performed every day until 3 days. At the end of the experiment, mice were euthanized by carbon dioxide asphyxiation and brains were collected for further analysis.

Intracranial injection

Mice were anaesthetized by intraperitoneal injection with (8.7 mg of ketamine + 1.3 mg of xylazine)/100 g. The mouse was then placed in the stereotaxic frame and fixed. Eye ointment was used to keep the mouse's eyes moist during the operation. The scalp was wiped several times with a sterile gauze soaked in chlorhexidine solution. A sagittal incision over the parieto-occipital bone (approximately 1-cm long) was completed using a sterile scalpel. The exposed skull surface was then cleaned using a cotton swab soaked in a 3% hydrogen peroxide solution. The micro-syringe (26 gauge, Hamilton) was positioned directly over the bregma after it was secured onto the micro-syringe pump (Harvard Apparatus, 11 Elite Nanomite). Before tumor cell injection, control knobs on the stereotaxic unit and a sterile variable speed rotary drill were used to puncture the skull at 2 mm to the right of the bregma and 1-mm anterior to the coronal suture, creating an opening for the injection of tumor cells. The cell suspension was gently mixed and drawn into the syringe using the pump controller while avoiding bubbles and clumps. The needle was inserted slowly to a depth of 4 mm. The injection volume was 3 μl, and the injection rate was set to 0.25 μl/min. After being in the brain for 1 to 2 min, the needle was gently removed from the tissue (for 3 to 4 min). Postoperative wound care and pain management were implemented, including wound closure and pain relief measures.

Orthotopic injection

Mice were anesthetized by intraperitoneal injection with (8.7 mg of ketamine + 1.3 mg of xylazine)/100 g. The operation area was disinfected with 2% chlorhexidine solution. The cell and Matrigel mixture were injected into the fat pad. The growth of primary tumors was monitored using bioluminescence imaging until surgical resection. The average time of this experiment was about 8 to 12 weeks. At the end point of the study, mice were euthanized by carbon dioxide asphyxiation, and primary tumors were harvested for following experiments.

Bioluminescence imaging

Mice were administrated intraperitoneally with 300 μl of 25 mM D-luciferin sodium salt (Abcam) in Dulbecco's PBS (Hyclone), anesthetized, and imaged at 20 min after injection using the IVIS Lumina Series III preclinical in vivo animal imaging system (PerkinElmer). For ex vivo imaging of bioluminescence signals in the brain, mice were administrated intraperitoneally with 300 μl of 25 mM D-luciferin and then euthanized with sodium pentobarbital. Brains were retrieved and placed in separate wells of a 12-well plate. Images were captured 1 min after adding 1 ml of D-luciferin (300 μg/ml) into each well to cover the tissue.

Cryostats section

For xenograft tissue cryostats section, the harvested tumor was washed with PBS, then embedded with optimal cutting temperature compound (Sakura), and frozen in the liquid nitrogen. Leica CM1950 cryostats was used to cut frozen sample blocks into 10-μm sections at −20°C, after that tissue sections were transferred to poly-L-lysine–coated glass bottom dish or positively charged glass slides and immersed in PBS with 1% proteinase inhibitors (Beyotime) for following analysis.

Magnetic-activated cell sorting

Magnetic-activated cell sorting (MACS) was adopted to select cancer cells from digested xenograft cells. Mouse Cell Depletion Kit (Miltenyibiotec) and MACS platform consisting of MidiMACS Separator, MACS MultiStand, and LS columns were used strictly following the manufactory's instructions. In detail, centrifuged cell mixtures were resuspended in 0.5% BSA-contained PBS buffer, and then mouse cell depletion cocktail was added and incubated at 2° to 8°C. After incubation, cell mixtures were added into buffer-prerinsed LS columns installed on MACS Separator and MultiStand for isolation and collection.

Fluorescence-activated cell sorting

Fluorescence-activated cell sorting (FACS) was used to separate cell populations based on fluorescence level. For preparation, cell suspensions were filtered with cell strains into single cells. After that, cell samples resuspended in PBS were loaded into BD FACSAria III Cell Sorter (BD Biosciences) following the instruction of the instrument. The sorted cells were collected into DMEM for later analysis. For some specific experiment design, mCherry$^{high/low}$ pNDRG1-mCherry cell harvested from TCP were defined as the 10% of the brightest/darkest populations; mCherry$^{+/-}$ pNDRG1-mCherry cells obtained from xenografts were gated on the basis of the expression level of mCherry of the same clone harvested from 0.6/35 kPa of PA gel.

Immunofluorescence staining

The cells or tumor cryostats sections were fixed with prechilled 4% PFA for 20 min at room temperature, followed by permeabilization with 0.3% Triton X-100 in PBS for 20 min. After being washed with PBS, cells were blocked with 1% BSA and glycine (22.52 mg/ml) in PBS containing 0.1% Tween 20 (PBST) for 1 hour at room temperature. Next, the cells were incubated with diluted primary antibodies in 1% BSA in PBST overnight at 4°C, washed three times with PBST for 5 min each time, and incubated with diluted secondary antibodies in 1% BSA in PBST at room temperature. After decanting the solution and washing the cells three times with PBST, nuclei were stained with DAPI. The imaging of cells was performed with a confocal microscope (Leica, TCS SPE) using 40× and 63× objectives. For F-actin staining, the CytoPainter F-actin labeling kit (Abcam, #ab112125) was used as per the user guidebook. Images were taken using the confocal microscope or the inverted fluorescence microscope. Quantification of fluorescence intensity was analyzed using the ImageJ software.

For the staining of brain slices, mice were euthanized after being anesthetized and then immediately perfused with PBS and 4% PFA and fixed overnight at 4°C. The brain was sectioned into 40- or 80-μm slices using a vibrating microtome. The prepared brain slices were treated with blocking buffer (0.3% Triton X-100 and 5% goat serum in PBS) for 1 hour at room temperature. Then, the brain slices were incubated with primary antibodies diluted in blocking buffer overnight at 4°C with or without Lectin-DyLight 649 (10 μg/ml; Thermo Fisher Scientific, #L32472). Following extensive washing with PBS, the fluorophore-conjugated secondary antibodies were diluted in blocking buffer and incubated for 2 hours at room temperature. After nuclei were stained, the brain sections were scanned or visualized with the inverted fluorescent microscope and confocal microscope using 10×, 20×, and 40× objectives. For 3D reconstruction, confocal images were captured every 2-μm interval for a total of 60-μm maximum at depth. ImageJ was used to analyze images, and Imaris was used to generate 3D reconstruction images.

The primary antibodies used in the study included p-MLC (1:50; Cell Signaling Technology, #3671), HDAC3 (1:500; Abcam, #ab32369),

Runx-2 (1:200; Abcam, #ab23981), SerpinB2 (1:200; Abcam, #ab47742), mCherry (1:100; Invitrogen, #m11217), and Ki-67 (1:200; Abcam, #ab15580). The secondary antibodies included Alexa Fluor 594 goat anti-mouse IgG H&L (1:400; Abcam, # ab150116), tetramethyl rhodamine isothiocyanate goat anti-rat IgG H + L (1:1000; Invitrogen, #26-4826-82), and Alexa Fluor 647 goat anti-mouse IgG H&L (1:400; Abcam, #ab15011).

Traction force microscope

The traction force of cells was measured using a protocol based on previous studies (*78*, *79*). First, an amino-silanated glass bottom of a confocal dish (NEST Scientific) and PA gels mixed with 0.2-μm diameter red fluorescence microspheres (Invitrogen, #F8763) were prepared as per PA gel preparation protocol. Next, cells were seeded on the PA gels and incubated for 24 hours. The prestressed state of the PA gel was captured by an inverted fluorescence microscope with a 20× magnification at the red fluorescence channel, and the boundary of cells was recorded by changing the imaging mode to bright field without moving the microscope stage. Then, the cells were lysed by adding TRK lysis buffer (Omega, #PR021) carefully and gently, and the image of microspheres beneath the cell was captured to represent the null-stress state of the PA gel. The images of prestressed and null-stress states were used to calculate the displacement maps of microspheres due to cellular contractility. The value of cell traction force was computed using the inverse Boussinesq mathematical model-based MATLAB algorithm based on the displacement map.

CCP measurement

To assess chromatin condensation, cells were seeded on the corresponding substrate for at least 24 hours and then fixed in precold 4% PFA for 15 min at room temperature. After being washed three times with PBS, nuclei were stained with DAPI and imaged at their midsection using confocal microscopy with 63× objectives. The gradient-based Sobel edge detection algorithm in MATLAB was used to process images to produce an edge map and calculate edge density representing the CCP, as described in a previous study (*49*). To reduce the impact of different fluorescence intensities of each nuclear image, the intensity of each pixel of the image was divided by the highest intensity of the image and multiplied by 255, after converting the image to an 8-bit image. The gradient-based Sobel edge detection algorithm was conducted to find the hasty reduction in intensity or strong edges associated with the degree of chromatin condensation. The thinning morphological algorithm was processed to count the number of sharp edges in the nucleus. The CCP of the nucleus was calculated by dividing the number of edges by the area of the nucleus. The images of heterochromatin regions in the nucleus were obtained following the adjusted threshold method reported in a previous study (*80*). The formula used to compute the adjusted threshold of heterochromatin was Mean of ($0.4 \times$ max) and min + [0.35 (max − min)], where max and min represented the maximum and minimum value of the pixel intensity of images, respectively. After this process, images of heterochromatin were converted into green color and then stacked with nuclear images marked by red color. All the image processing was conducted using ImageJ.

HDACs activity measurement

The activity of HDAC enzymes in cells was measured using an in situ HDAC activity fluorometric assay kit (EPI003, Sigma-Aldrich) according to the manufacture's protocol. A total of 50,000 cells per well were seeded in a 24-well plate with or without PA gels. After incubation for 24 hours, the culture medium was removed, and 300 μl of reaction mixture was added to each well. Following incubation at standard cell culture conditions for 2 hours, 300 μl of developer solution was added, and cells were further incubated for 30 min. The supernatant was then transferred to a black 96-well plate with a transparent bottom, and fluorescence was detected using a Varioskan LUX multimode microplate reader (Thermo Fisher Scientific) at an excitation/emission wavelength of 368/442 nm.

HDAC3 activity measurement

For immunoprecipitations, cells were washed with ice-cold PBS and then lysed in a nondenaturing lysis buffer (Solarbio, #R0030) supplemented with a cocktail of protease inhibitors. The protein concentrations in the cell lysates were measured using bicinchoninic acid (BCA) assay and then adjusted to the same level for consistency among samples. The cell lysates were subjected to immunoprecipitation using the HDAC3 primary antibody (Abcam, #ab13770) overnight at 4°C with gentle rotation. The immunocomplexes were subsequently collected by incubating the lysates with protein-A/G beads (Abcam, #ab193262) for 2 hours, followed by four washes to remove nonspecific binding. HDAC3 activities were measured from the immunoprecipitated samples using a HDAC fluorometric kit (Abcam, #ab156064).

Pharmacologic treatment

For pharmacologic treatment, cells were grown until 50 to 70% confluency and then treated with various compounds. Y-27632 (Selleck Chemicals) at 2 or 6 μM, blebbistatin (Sigma-Aldrich) at 2 or 6 μM, vorinostat (SAHA; Selleck Chemicals) at 2 μM, anacardic acid (Selleck Chemicals) at 50 μM, TSA (MedChemExpress) at 100 nM, cytochalasin D (Tocris Bioscience) at 0.1 or 0.3 μM, Narci (Selleck Chemicals) at 5, 10, or 50 nM, Jas (Selleck Chemicals) at 30 or 100 nM, and RGFP966 (MedChemExpress) at 1 μM or 10 μM were used for the indicated time periods. All compounds were obtained as stock solutions in dimethyl sulfoxide (DMSO) according to the manufacturer's recommendations and then diluted with full cell culture medium to obtain the working solutions. DMSO was used as the vehicle for the control treatment. For the animal study, mice were treated every 2 days with vehicle and RGFP966 (10 mg/kg or 40 mg/kg) intraperitoneally. RGFP966 was dissolved in a vehicle solution consisting of 10% DMSO and 45% PEG 400 in water.

Ex vivo luciferase activity assay

A total of 200 mg of freshly resected brain was snap-frozen and individually homogenized with Precellys Evolution Homogenizer (Bertin Technologies). A total of 200 μl of reporter lysis buffer (Promega) was added into sample tubes and mixed well. Alternating freeze and thaw was performed three times with liquid nitrogen and 37°C water bath. Then, the samples were centrifuged at 14,000 rpm for 10 min at 4°C. Each 20 μl of supernatant was mixed with 100 μl of luciferase assay reagent (Promega), and the luciferase activity was measured by Varioskan LUX multimode microplate reader (Thermo Fisher Scientific).

Transfection with siRNAs and plasmids

Small interfering RNAs (siRNAs) and plasmids were transfected into the cells using Lipofectamine 3000 transfection reagent (Invitrogen) according to the manufacturer's instructions. Briefly, cells were trypsinized and seeded until they reached 70 to 80% confluency on the

day of transfection. The Lipofectamine 3000 reagent was thoroughly mixed with Opti-MEM reduced serum medium (Gibco) at the recommended ratio. Then, the siRNA or plasmid was diluted in Opti-MEM–reduced serum medium with or without the P3000 reagent and then mixed with equal volume of the prepared Lipofectamine 3000 solution. After 15 min at room temperature, this mixture was added to the cells for transfection (250 μl for one well of six-well plate). All siRNAs were designed and produced by General Biosystems, and their efficiency was verified by quantitative PCR (qPCR). The HDAC3-Flag plasmid (Addgene, #13819) was obtained from Addgene.

Lentiviral transduction and stable cell line establishment

293T cells were cotransfected with the target plasmid, the psPAX2 packaging plasmid (Addgene, #12260), and the pMD2.G envelope plasmid (Addgene, #12259) using Lipofectamine 3000. Culture supernatant containing virus was collected at 48 and 72 hours post-transfection, filtered through a 0.45-μm filter, and concentrated using a virus concentration kit (Beyotime, C2901S). Tumor cells were then transduced by adding the concentrated lentivirus solution to the complete medium containing polybrene (8 μg/ml) overnight. After 48 hours, stable cell lines were selected using G418 (500 μg/ml; Sigma-Aldrich) or puromycin (2 μg/ml; MedChemExpress) and then further sorted using a FACSAria III Cell Sorter (BD).

The used plasmids included (i) pLV-mCherry: T2A: Puro-EF1A > hHDAC3 (VectorBuilder), (ii) pLV-mCherry/Puro-EF1A > ORF (VectorBuilder); (iii) pinducer 20 DN-KASH (Addgene, #125554); and (iv) pinducer 20 DN-KASHΔPPPL (Addgene, #129280). HDAC S424A and pNDRG1-mCherry plasmid was synthesized by Yanming Biotech. The promoter of the NDRG1 gene was defined as the 2000–base pair upstream of the start codon based on NCBI database, and the NDRG1 promoter was recombined into the upstream of mCherry gene in pLVX-mCherry-C1(Cla l–Xho l) vector to drive the transcription.

Statistical analysis

All results were presented as means ± SEM from at least three independent experiments. Comparisons between two groups were analyzed using an unpaired two-tailed Student's *t* test or Mann-Whitney test. For comparisons of more than two groups, Welch and Brown-Forsythe one-way analysis of variance (ANOVA) with a relevant post hoc test or Kruskal-Wallis test was performed. Differences in Kaplan-Meier curves were evaluated using the log-rank test. All statistical analyses were conducted using GraphPad Prism 8.0 software, and *P* value less than 0.05 was considered statistically significant.

Supplementary Materials

This PDF file includes:

Figs. S1 to S18
Tables S1 and S2

REFERENCES AND NOTES

1. Y. Gao, I. Bado, H. Wang, W. Zhang, J. M. Rosen, X. H.-F. Zhang, Metastasis organotropism: Redefining the congenial soil. *Dev. Cell* **49**, 375–391 (2019).
2. A. S. Achrol, R. C. Rennert, C. Anders, R. Soffietti, M. S. Ahluwalia, L. Nayak, S. Peters, N. D. Arvold, G. R. Harsh, P. S. Steeg, S. D. Chang, Brain metastases. *Nat. Rev. Dis. Primers.* **5**, 5 (2019).
3. R. Kotecha, V. Gondi, M. S. Ahluwalia, P. K. Brastianos, M. P. Mehta, Recent advances in managing brain metastasis. *F1000Res.* **7**, 1772 (2018).
4. I. Witzel, L. Oliveira-Ferrer, K. Pantel, V. Muller, H. Wikman, Breast cancer brain metastases: Biology and new clinical perspectives. *Breast Cancer Res.* **18**, 8 (2016).
5. C. Bachmann, S. Schmidt, A. Staebler, T. Fehm, F. Fend, J. Schittenhelm, D. Wallwiener, E. Grischke, CNS metastases in breast cancer patients: Prognostic implications of tumor subtype. *Med. Oncol.* **32**, 400 (2015).
6. N. J. Birkbak, N. McGranahan, Cancer genome evolutionary trajectories in metastasis. *Cancer Cell* **37**, 8–19 (2020).
7. A. C. Chiang, J. Massague, Molecular basis of metastasis. *N. Engl. J. Med.* **359**, 2814–2823 (2008).
8. D. Padua, X. H.-F. Zhang, Q. Wang, C. Nadal, W. L. Gerald, R. R. Gomis, J. Massagué, TGFβ primes breast tumors for lung metastasis seeding through angiopoietin-like 4. *Cell* **133**, 66–77 (2008).
9. X. H.-F. Zhang, X. Jin, S. Malladi, Y. Zou, Y. H. Wen, E. Brogi, M. Smid, J. A. Foekens, J. Massagué, Selection of bone metastasis seeds by mesenchymal signals in the primary tumor stroma. *Cell* **154**, 1060–1073 (2013).
10. A. Hoshino, B. Costa-Silva, T. L. Shen, G. Rodrigues, A. Hashimoto, M. Tesic Mark, H. Molina, S. Kohsaka, A. Di Giannatale, S. Ceder, S. Singh, C. Williams, N. Soplop, K. Uryu, L. Pharmer, T. King, L. Bojmar, A. E. Davies, Y. Ararso, T. Zhang, H. Zhang, J. Hernandez, J. M. Weiss, V. D. Dumont-Cole, K. Kramer, L. H. Wexler, A. Narendran, G. K. Schwartz, J. H. Healey, P. Sandstrom, K. J. Labori, E. H. Kure, P. M. Grandgenett, M. A. Hollingsworth, M. de Sousa, S. Kaur, M. Jain, K. Mallya, S. K. Batra, W. R. Jarnagin, M. S. Brady, O. Fodstad, V. Muller, K. Pantel, A. J. Minn, M. J. Bissell, B. A. Garcia, Y. Kang, V. K. Rajasekhar, C. M. Ghajar, I. Matei, H. Peinado, J. Bromberg, D. Lyden, Tumour exosome integrins determine organotropic metastasis. *Nature* **527**, 329–335 (2015).
11. Y. Jin, Y. Kang, M. Wang, B. Wu, B. Su, H. Yin, Y. Tang, Q. Li, W. Wei, Q. Mei, G. Hu, V. Lukacs-Kornek, J. Li, K. Wu, X. Yuan, W. Wang, Targeting polarized phenotype of microglia via IL6/JAK2/STAT3 signaling to reduce NSCLC brain metastasis. *Signal Transduct. Target. Ther.* **7**, 52 (2022).
12. H. T. Nia, L. L. Munn, R. K. Jain, Physical traits of cancer. *Science* **370**, eaaz0868 (2020).
13. M. J. Paszek, N. Zahir, K. R. Johnson, J. N. Lakins, G. I. Rozenberg, A. Gefen, C. A. Reinhart-King, S. S. Margulies, M. Dembo, D. Boettiger, D. A. Hammer, V. M. Weaver, Tensional homeostasis and the malignant phenotype. *Cancer Cell* **8**, 241–254 (2005).
14. S. C. Wei, L. Fattet, J. H. Tsai, Y. Guo, V. H. Pai, H. E. Majeski, A. C. Chen, R. L. Sah, S. S. Taylor, A. J. Engler, J. Yang, Matrix stiffness drives epithelial-mesenchymal transition and tumour metastasis through a TWIST1-G3BP2 mechanotransduction pathway. *Nat. Cell Biol.* **17**, 678–688 (2015).
15. W. Wang, P. V. Taufalele, M. Millet, K. Homsy, K. Smart, E. D. Berestesky, C. T. Schunk, M. M. Rowe, F. Bordeleau, C. A. Reinhart-King, Matrix stiffness regulates tumor cell intravasation through expression and ESRP1-mediated alternative splicing of MENA. *Cell Rep.* **42**, 112338 (2023).
16. S. E. Reid, E. J. Kay, L. J. Neilson, A. T. Henze, J. Serneels, E. J. McGhee, S. Dhayade, C. Nixon, J. B. Mackey, A. Santi, K. Swaminathan, D. Athineos, V. Papalazarou, F. Patella, A. Roman-Fernandez, Y. ElMaghloob, J. R. Hernandez-Fernaud, R. H. Adams, S. Ismail, D. M. Bryant, M. Salmeron-Sanchez, L. M. Machesky, L. M. Carlin, K. Blyth, M. Mazzone, S. Zanivan, Tumor matrix stiffness promotes metastatic cancer cell interaction with the endothelium. *EMBO J.* **36**, 2373–2389 (2017).
17. A. Malandrino, M. Mak, R. D. Kamm, E. Moeendarbary, Complex mechanics of the heterogeneous extracellular matrix in cancer. *Extreme Mech. Lett.* **21**, 25–34 (2018).
18. C. Liu, M. Li, Z. X. Dong, D. Jiang, X. Li, S. Lin, D. Chen, X. Zou, X. D. Zhang, G. D. Luker, Heterogeneous microenvironmental stiffness regulates pro-metastatic functions of breast cancer cells. *Acta Biomater.* **131**, 326–340 (2021).
19. J. Wei, J. Yao, C. Yang, Y. Mao, D. Zhu, Y. Xie, P. Liu, M. Yan, L. Ren, Y. Lin, Q. Zheng, X. Li, Heterogeneous matrix stiffness regulates the cancer stem-like cell phenotype in hepatocellular carcinoma. *J. Transl. Med.* **20**, 555 (2022).
20. C. Stashko, M. K. Hayward, J. J. Northey, N. Pearson, A. J. Ironside, J. N. Lakins, R. Oria, M. A. Goyette, L. Mayo, H. G. Russnes, E. S. Hwang, M. L. Kutys, K. Polyak, V. M. Weaver, A convolutional neural network STIFMap reveals associations between stromal stiffness and EMT in breast cancer. *Nat. Commun.* **14**, 3561 (2023).
21. A. Kostic, C. D. Lynch, M. P. Sheetz, Differential matrix rigidity response in breast cancer cell lines correlates with the tissue tropism. *PLOS ONE* **4**, e6361 (2009).
22. D. J. McGrail, Q. M. Kieu, J. A. Iandoli, M. R. Dawson, Actomyosin tension as a determinant of metastatic cancer mechanical tropism. *Phys. Biol.* **12**, 026001 (2015).
23. R. V. Kondapaneni, S. S. Rao, Matrix stiffness and cluster size collectively regulate dormancy versus proliferation in brain metastatic breast cancer cell clusters. *Biomater. Sci.* **8**, 6637–6646 (2020).
24. J. M. Page, A. R. Merkel, N. S. Ruppender, R. Guo, U. C. Dadwal, S. Cannonier, S. Basu, S. A. Guelcher, J. A. Sterling, Matrix rigidity regulates the transition of tumor cells to a bone-destructive phenotype through integrin β3 and TGF-β receptor type II. *Biomaterials* **64**, 33–44 (2015).
25. A. W. Watson, A. D. Grant, S. S. Parker, S. Hill, M. B. Whalen, J. Chakrabarti, M. W. Harman, M. R. Roman, B. L. Forte, C. C. Gowan, R. Castro-Portuguez, L. K. Stolze, C. Franck, D. A. Cusanovich, Y. Zavros, M. Padi, C. E. Romanoski, G. Mouneimne, Breast tumor stiffness instructs bone metastasis via maintenance of mechanical conditioning. *Cell Rep.* **35**, 109293 (2021).

26. Z. Liu, L. Wang, H. Xu, Q. Du, L. Li, L. Wang, E. S. Zhang, G. Chen, Y. Wang, Heterogeneous responses to mechanical force of prostate cancer cells inducing different metastasis patterns. *Adv. Sci.* **7**, 1903583 (2020).
27. M. Egeblad, M. G. Rasch, V. M. Weaver, Dynamic interplay between the collagen scaffold and tumor evolution. *Curr. Opin. Cell Biol.* **22**, 697–706 (2010).
28. J. J. Northey, A. S. Barrett, I. Acerbi, M. K. Hayward, S. Talamantes, I. S. Dean, J. K. Mouw, S. M. Ponik, J. N. Lakins, P. J. Huang, J. Wu, Q. Shi, S. Samson, P. J. Keely, R. A. Mukhtar, J. T. Liphardt, J. A. Shepherd, E. S. Hwang, Y. Y. Chen, K. C. Hansen, L. E. Littlepage, V. M. Weaver, Stiff stroma increases breast cancer risk by inducing the oncogene ZNF217. *J. Clin. Invest.* **130**, 5721–5737 (2020).
29. M. Plodinec, M. Loparic, C. A. Monnier, E. C. Obermann, R. Zanetti-Dallenbach, P. Oertle, J. T. Hyotyla, U. Aebi, M. Bentires-Alj, R. Y. H. Lim, C.-A. Schoenenberger, The nanomechanical signature of breast cancer. *Nat. Nanotechnol.* **7**, 757–765 (2012).
30. J. Neman, J. Termini, S. Wilczynski, N. Vaidehi, C. Choy, C. M. Kowolik, H. Li, A. C. Hambrecht, E. Roberts, R. Jandial, Human breast cancer metastases to the brain display GABAergic properties in the neural niche. *Proc. Natl. Acad. Sci. U.S.A.* **111**, 984–989 (2014).
31. E. Wingrove, Z. Z. Liu, K. D. Patel, A. Arnal-Estape, W. L. Cai, M.-A. Melnick, K. Politi, C. Monteiro, L. Zhu, M. Valiente, H. M. Kluger, V. L. Chiang, D. X. Nguyen, Transcriptomic hallmarks of tumor plasticity and stromal interactions in brain metastasis. *Cell Rep.* **27**, 1277–1292.e7 (2019).
32. Q. Huang, X. Hu, W. He, Y. Zhao, S. Hao, Q. Wu, S. Li, S. Zhang, M. Shi, Fluid shear stress and tumor metastasis. *Am. J. Cancer Res.* **8**, 763–777 (2018).
33. P. D. Bos, X. H.-F. Zhang, C. Nadal, W. Shu, R. R. Gomis, D. X. Nguyen, A. J. Minn, M. J. van de Vijver, W. L. Gerald, J. A. Foekens, J. Massagué, Genes that mediate breast cancer metastasis to the brain. *Nature* **459**, 1005–1009 (2009).
34. K. Wu, K. Fukuda, F. Xing, Y. Zhang, S. Sharma, Y. Liu, M. D. Chan, X. Zhou, S. A. Qasem, R. Pochampally, Y. Y. Mo, K. Watabe, Roles of the cyclooxygenase 2 matrix metalloproteinase 1 pathway in brain metastasis of breast cancer. *J. Biol. Chem.* **290**, 9842–9854 (2015).
35. M. B. Chen, J. A. Whisler, J. S. Jeon, R. D. Kamm, Mechanisms of tumor cell extravasation in an in vitro microvascular network platform. *Integr. Biol.* **5**, 1262–1271 (2013).
36. S. M. A. Arefi, D. Tsvirkun, C. Verdier, J. J. Feng, A biomechanical model for the transendothelial migration of cancer cells. *Phys. Biol.* **17**, 036004 (2020).
37. J. Escribano, M. B. Chen, E. Moeendarbary, X. Cao, V. Shenoy, J. M. Garcia-Aznar, R. D. Kamm, F. Spill, Balance of mechanical forces drives endothelial gap formation and may facilitate cancer and immune-cell extravasation. *PLOS Comput. Biol.* **15**, e1006395 (2019).
38. K. Tanner, Perspective: The role of mechanobiology in the etiology of brain metastasis. *APL Bioeng.* **2**, 031801 (2018).
39. J. Fares, A. Cordero, D. Kanojia, M. S. Lesniak, The network of cytokines in brain metastases. *Cancers* **13**, 142 (2021).
40. M. Valiente, A. C. Obenauf, X. Jin, Q. Chen, X. H. Zhang, D. J. Lee, J. E. Chaft, M. G. Kris, J. T. Huse, E. Brogi, J. Massagué, Serpins promote cancer cell survival and vascular co-option in brain metastasis. *Cell* **156**, 1002–1016 (2014).
41. Y. Kienast, L. von Baumgarten, M. Fuhrmann, W. E. Klinkert, R. Goldbrunner, J. Herms, F. Winkler, Real-time imaging reveals the single steps of brain metastasis formation. *Nat. Med.* **16**, 116–122 (2010).
42. Y. Xin, K. Li, M. Huang, C. Liang, D. Siemann, L. Wu, Y. Tan, X. Tang, Biophysics in tumor growth and progression: From single mechano-sensitive molecules to mechanomedicine. *Oncogene* **42**, 3457–3490 (2023).
43. X. Chen, Z. Xu, K. Tang, G. Hu, P. Du, J. Wang, C. Zhang, Y. Xin, K. Li, Q. Zhang, J. Hu, Z. Zhang, M. Yang, G. Wang, Y. Tan, The mechanics of tumor cells dictate malignancy via cytoskeleton-mediated APC/Wnt/β-catenin signaling. *Research* **6**, 0224 (2023).
44. J. Wang, B. Zhang, X. Chen, Y. Xin, K. Li, C. Zhang, K. Tang, Y. Tan, Cell mechanics regulate the migration and invasion of hepatocellular carcinoma cells via JNK signaling. *Acta Biomater.* **176**, 321–333 (2024).
45. T. C. Wang, S. Sawhney, D. Morgan, R. L. Bennett, R. Rashmi, M. R. Estecio, A. Brock, I. Singh, C. F. Baer, J. D. Licht, T. P. Lele, Genetic variation drives cancer cell adaptation to ECM stiffness. *Proc. Natl. Acad. Sci. U.S.A.* **121**, e2403062121 (2024).
46. M. M. Nava, Y. A. Miroshnikova, L. C. Biggs, D. B. Whitefield, F. Metge, J. Boucas, H. Vihinen, E. Jokitalo, X. Li, J. M. Garcia Arcos, B. Hoffmann, R. Merkel, C. M. Niessen, K. N. Dahl, S. A. Wickstrom, Heterochromatin-driven nuclear softening protects the genome against mechanical stress-induced damage. *Cell* **181**, 800–817.e22 (2020).
47. F. Alisafaei, D. S. Jokhun, G. V. Shivashankar, V. B. Shenoy, Regulation of nuclear architecture, mechanics, and nucleocytoplasmic shuttling of epigenetic factors by cell geometric constraints. *Proc. Natl. Acad. Sci. U.S.A.* **116**, 13200–13209 (2019).
48. C. J. Millard, P. J. Watson, I. Celardo, Y. Gordiyenko, S. M. Cowley, C. V. Robinson, L. Fairall, J. W. R. Schwabe, Class I HDACs share a common mechanism of regulation by inositol phosphates. *Mol. Cell* **51**, 57–67 (2013).
49. J. Irianto, D. A. Lee, M. M. Knight, Quantification of chromatin condensation level by image processing. *Med. Eng. Phys.* **36**, 412–417 (2014).
50. B. Fu, J. Shen, X. Zou, N. Sun, Z. Zhang, Z. Liu, C. Zeng, H. Liu, W. Huang, Matrix stiffening promotes chondrocyte senescence and the osteoarthritis development through downregulating *HDAC3*. *Bone Res.* **12**, 32 (2024).
51. X. Xu, H. Zhang, Y. Li, F. Liu, Z. Jing, M. Ren, T. Chen, Y. Fu, Y. Wu, P. Ji, S. Yang, Chromatin remodeling and nucleoskeleton synergistically control osteogenic differentiation in different matrix stiffnesses. *Mater. Today Bio.* **20**, 100661 (2023).
52. J. F. Huang, J. Shen, X. Li, R. Rengan, N. Silvestris, M. Wang, L. Derosa, X. Zheng, A. Belli, X. L. Zhang, Y. M. Li, A. Wu, Incidence of patients with bone metastases at diagnosis of solid tumors in adults: A large population-based study. *Ann. Transl. Med.* **8**, 482 (2020).
53. M. J. Zhang, Q. C. Zhao, M. X. Xia, J. Chen, Y. T. Chen, X. Cao, Y. Liu, Z. Q. Yuan, X. Y. Wang, Y. Xu, The HDAC3 inhibitor RGFP966 ameliorated ischemic brain damage by downregulating the AIM2 inflammasome. *FASEB J.* **34**, 648–662 (2020).
54. A. R. Killaars, C. J. Walker, K. S. Anseth, Nuclear mechanosensing controls MSC osteogenic potential through HDAC epigenetic remodeling. *Proc. Natl. Acad. Sci. U.S.A.* **117**, 21258–21266 (2020).
55. C. R. Mayer, P. T. Arsenovic, K. Bathula, K. B. Denis, D. E. Conway, Characterization of 3D printed stretching devices for imaging force transmission in live-cells. *Cell. Mol. Bioeng.* **12**, 289–300 (2019).
56. P. M. Davidson, A. Battistella, T. Dejardin, T. Betz, J. Plastino, N. Borghi, B. Cadot, C. Sykes, Nesprin-2 accumulates at the front of the nucleus during confined cell migration. *EMBO Rep.* **21**, e49910 (2020).
57. S. Dupont, L. Morsut, M. Aragona, E. Enzo, S. Giulitti, M. Cordenonsi, F. Zanconato, J. Le Digabel, M. Forcato, S. Bicciato, N. Elvassore, S. Piccolo, Role of YAP/TAZ in mechanotransduction. *Nature* **474**, 179–183 (2011).
58. M. Valiente, A. E. D. Van Swearingen, C. K. Anders, A. Bairoch, A. Boire, P. D. Bos, D. M. Cittelly, N. Erez, G. B. Ferraro, D. Fukumura, B. Gril, M. Herlyn, S. L. Holmen, R. K. Jain, J. A. Joyce, M. Lorger, J. Massague, J. Neman, N. R. Sibson, P. S. Steeg, F. Thorsen, L. S. Young, D. Vareslija, A. Vultur, F. Weis-Garcia, F. Winkler, Brain metastasis cell lines panel: A public resource of organotropic cell lines. *Cancer Res.* **80**, 4314–4323 (2020).
59. T. Panciera, A. Citron, D. Di Biagio, G. Battilana, A. Gandin, S. Giulitti, M. Forcato, S. Bicciato, V. Panzetta, S. Fusco, L. Azzolin, A. Totaro, A. P. Dei Tos, M. Fassan, V. Vindigni, F. Bassetto, A. Rosato, G. Brusatin, M. Cordenonsi, S. Piccolo, Reprogramming normal cells into tumour precursors requires ECM stiffness and oncogene-mediated changes of cell mechanical properties. *Nat. Mater.* **19**, 797–806 (2020).
60. R. Reuten, S. Zendehroud, M. Nicolau, L. Fleischhauer, A. Laitala, S. Kiderlen, D. Nikodemus, L. Wullkopf, S. R. Nielsen, S. McNeilly, C. Prein, M. Rafaeva, E. M. Schoof, B. Furtwangler, B. T. Porse, H. Kim, K. J. Won, S. Sudhop, K. W. Zornhagen, F. Suhr, E. Maniati, O. M. T. Pearce, M. Koch, L. B. Oddershede, T. Van Agtmael, C. D. Madsen, A. E. Mayorca-Guiliani, W. Bloch, R. R. Netz, H. Clausen-Schaumann, J. T. Erler, Basement membrane stiffness determines metastases formation. *Nat. Mater.* **20**, 892–903 (2021).
61. M. Kalli, M. D. Poskus, T. Stylianopoulos, I. K. Zervantonakis, Beyond matrix stiffness: Targeting force-induced cancer drug resistance. *Trends Cancer* **9**, 937–954 (2023).
62. Q. Zeng, I. P. Michael, P. Zhang, S. Saghafinia, G. Knott, W. Jiao, B. D. McCabe, J. A. Galvan, H. P. C. Robinson, I. Zlobec, G. Ciriello, D. Hanahan, Synaptic proximity enables NMDAR signalling to promote brain metastasis. *Nature* **573**, 526–531 (2019).
63. S. Teng, Y. E. Li, M. Yang, R. Qi, Y. Huang, Q. Wang, Y. Zhang, S. Chen, S. Li, K. Lin, Y. Cao, Q. Ji, Q. Gu, Y. Cheng, Z. Chang, W. Guo, P. Wang, I. Garcia-Bassets, Z. J. Lu, D. Wang, Tissue-specific transcription reprogramming promotes liver metastasis of colorectal cancer. *Cell Res.* **30**, 34–49 (2020).
64. J. Baek, P. A. Lopez, S. Lee, T. S. Kim, S. Kumar, D. V. Schaffer, Egr1 is a 3D matrix-specific mediator of mechanosensitive stem cell lineage commitment. *Sci. Adv.* **8**, eabm4646 (2022).
65. A. J. Engler, S. Sen, H. L. Sweeney, D. E. Discher, Matrix elasticity directs stem cell lineage specification. *Cell* **126**, 677–689 (2006).
66. L. Ma, L. Qi, S. Li, Q. Yin, J. Liu, J. Wang, C. She, P. Li, Q. Liu, X. Wang, W. Li, Aberrant HDAC3 expression correlates with brain metastasis in breast cancer patients. *Thorac. Cancer* **11**, 2493–2505 (2020).
67. D. Palmieri, P. R. Lockman, F. C. Thomas, E. Hua, J. Herring, E. Hargrave, M. Johnson, N. Flores, Y. Qian, E. Vega-Valle, K. S. Taskar, V. Rudraraju, R. K. Mittapalli, J. A. Gaasch, K. A. Bohn, H. R. Thorsheim, D. J. Liewehr, S. Davis, J. F. Reilly, R. Walker, J. L. Bronder, L. Feigenbaum, S. M. Steinberg, K. Camphausen, P. S. Meltzer, V. M. Richon, Q. R. Smith, P. S. Steeg, Vorinostat inhibits brain metastatic colonization in a model of triple-negative breast cancer and induces DNA double-strand breaks. *Clin. Cancer Res.* **15**, 6148–6157 (2009).
68. K. Qu, L. C. Zaba, A. T. Satpathy, P. G. Giresi, R. Li, Y. Jin, R. Armstrong, C. Jin, N. Schmitt, Z. Rahbar, H. Ueno, W. J. Greenleaf, Y. H. Kim, H. Y. Chang, Chromatin accessibility landscape of cutaneous T cell lymphoma and dynamic response to HDAC inhibitors. *Cancer Cell* **32**, 27–41.e4 (2017).
69. A. Nott, J. Cheng, F. Gao, Y. T. Lin, E. Gjoneska, T. Ko, P. Minhas, A. V. Zamudio, J. Meng, F. Zhang, P. Jin, L. H. Tsai, Histone deacetylase 3 associates with MeCP2 to regulate FOXO and social behavior. *Nat. Neurosci.* **19**, 1497–1505 (2016).
70. J. Demmerle, A. J. Koch, J. M. Holaska, The nuclear envelope protein emerin binds directly to histone deacetylase 3 (HDAC3) and activates HDAC3 activity. *J. Biol. Chem.* **287**, 22080–22088 (2012).

71. R. Somech, S. Shaklai, O. Geller, N. Amariglio, A. J. Simon, G. Rechavi, E. N. Gal-Yam, The nuclear-envelope protein and transcriptional repressor LAP2beta interacts with HDAC3 at the nuclear periphery, and induces histone H4 deacetylation. *J. Cell Sci.* **118**, 4017–4025 (2005).
72. J. R. Tse, A. J. Engler, Preparation of hydrogel substrates with tunable mechanical properties. *Curr. Protoc. Cell Biol.* **47**, 10.16.1–10.16.16 (2010).
73. Z. Xun, X. Ding, Y. Zhang, B. Zhang, S. Lai, D. Zou, J. Zheng, G. Chen, B. Su, L. Han, Y. Ye, Reconstruction of the tumor spatial microenvironment along the malignant-boundary-nonmalignant axis. *Nat. Commun.* **14**, 933 (2023).
74. Y. Xin, X. Chen, X. Tang, K. Li, M. Yang, W. C. Tai, Y. Liu, Y. Tan, Mechanics and actomyosin-dependent survival/chemoresistance of suspended tumor cells in shear flow. *Biophys. J.* **116**, 1803–1814 (2019).
75. B. Zhang, X. Li, K. Tang, Y. Xin, G. Hu, Y. Zheng, K. Li, C. Zhang, Y. Tan, Adhesion to the brain endothelium selects breast cancer cells with brain metastasis potential. *Int. J. Mol. Sci.* **24**, 7087 (2023).
76. K. Y. Ng, Q. T. Shea, T. L. Wong, S. T. Luk, M. Tong, C. M. Lo, K. Man, J. P. Yun, X. Y. Guan, T. K. Lee, Y. P. Zheng, S. Ma, Chemotherapy-enriched THBS2-deficient cancer stem cells drive hepatocarcinogenesis through matrix softness induced histone H3 modifications. *Adv. Sci.* **8**, 2002483 (2021).
77. F. Polleux, A. Ghosh, The slice overlay assay: A versatile tool to study the influence of extracellular signals on neuronal development. *Sci. STKE* **2002**, pl9 (2002).
78. J. Liu, Y. Tan, H. Zhang, Y. Zhang, P. Xu, J. Chen, Y. C. Poh, K. Tang, N. Wang, B. Huang, Soft fibrin gels promote selection and growth of tumorigenic cells. *Nat. Mater.* **11**, 734–741 (2012).
79. J. Jin, K. Tang, Y. Xin, T. Zhang, Y. Tan, Hemodynamic shear flow regulates biophysical characteristics and functions of circulating breast tumor cells reminiscent of brain metastasis. *Soft Matter* **14**, 9528–9533 (2018).
80. K. Damodaran, S. Venkatachalapathy, F. Alisafaei, A. V. Radhakrishnan, D. Sharma Jokhun, V. B. Shenoy, G. V. Shivashankar, Compressive force induces reversible chromatin condensation and cell geometry-dependent transcriptional response. *Mol. Biol. Cell* **29**, 3039–3051 (2018).

Acknowledgments: We thank T. Zhu in L. Sun's group (Hong Kong Polytechnic University) for providing the training of intracranial injection and the University Life Science Facility and the University Research Facility in Behavioral and Systems Neuroscience in the Hong Kong Polytechnic University for providing confocal laser scanning microscopy, IVIS imaging system, flow cytometry, vibratome, and centralized animal facility for this study. **Funding:** This work was supported by the National Natural Science Foundation of China (project no. 11972316 to Y.T.), the Shenzhen Science and Technology Innovation Commission (project no. JCYJ20200109142001798, SGDX2020110309520303, and JCYJ20220531091002006 to Y.T.), the Hong Kong Research Grant Council (PolyU 15214320, 15227523, and C5016-23G to Y.T.), the Health and Medical Research Fund (HMRF18191421 to Y.T.), the Nankai University Institute of Ophthalmology (NKYKD202205 to Y.T.), the Research Institute for Smart Ageing in Hong Kong Polytechnic University (1-CD75 to Y.T.), and the Hong Kong Polytechnic University (1-ZE2M and 1-ZVY1 to Y.T.). **Author contributions:** Conceptualization: Y.T. Methodology: K.T. and Y.Z. Investigation: K.T., Y.Z., G.H., Y.X., K.L., C.Z., X.C. B.Z., X.L., B.H., and Q.J. Visualization: K.T. Supervision: Y.T., Y.-p. Z., and M.Y. Writing—original draft: Y.T., K.T., and Y.Z. Writing—review and editing: Y.T. and K.T. **Competing interests:** The authors declare that they have no competing interests. **Data and materials availability:** All data needed to evaluate the conclusions in the paper are present in the paper and/or the Supplementary Materials. The previously published RNA-seq data that we reanalyzed for this study are available from the National Center for Biotechnology information (NCBI) Gene Expression Omnibus (GEO; www.ncbi.nlm.nih.gov/geo/) under indicated accession numbers (GSE127887 and GSE210616_GSM6433585).

Submitted 6 May 2024
Accepted 23 January 2025
Published 26 February 2025
10.1126/sciadv.adq2881